MOLECULAR BIOLOGY

A common genetic variant of a mitochondrial RNA processing enzyme predisposes to insulin resistance

Giulia Rossetti[1,2,3], Judith A. Ermer[1,2,3], Maike Stentenbach[1,2,3], Stefan J. Siira[1,2,3], Tara R. Richman[1,2,3], Dusanka Milenkovic[4], Kara L. Perks[1,2,3], Laetitia A. Hughes[1,2,3], Emma Jamieson[5], Gulibaikelamu Xiafukaiti[6], Natalie C. Ward[7], Satoru Takahashi[6], Nicola Gray[8], Helena M. Viola[9], Livia C. Hool[9,10], Oliver Rackham[1,2,11,12,13], Aleksandra Filipovska[1,2,3,13,14]*

Mitochondrial energy metabolism plays an important role in the pathophysiology of insulin resistance. Recently, a missense N437S variant was identified in the *MRPP3* gene, which encodes a mitochondrial RNA processing enzyme within the RNase P complex, with predicted impact on metabolism. We used CRISPR-Cas9 genome editing to introduce this variant into the mouse *Mrpp3* gene and show that the variant causes insulin resistance on a high-fat diet. The variant did not influence mitochondrial gene expression markedly, but instead, it reduced mitochondrial calcium that lowered insulin release from the pancreatic islet β cells of the *Mrpp3* variant mice. Reduced insulin secretion resulted in lower insulin levels that contributed to imbalanced metabolism and liver steatosis in the *Mrpp3* variant mice on a high-fat diet. Our findings reveal that the MRPP3 variant may be a predisposing factor to insulin resistance and metabolic disease in the human population.

INTRODUCTION

Insulin resistance and impaired insulin secretion are the main defects in type 2 diabetes, projected to be the seventh leading cause of death by 2030 (*1*). Impaired energy production, use of energy stores, and mitochondrial dysfunction are major features in metabolic diseases. Nevertheless, it remains uncertain how mitochondrial dysfunction can cause, contribute to, or result in insulin resistance and metabolic disease. Mutations and variations in genes encoding mitochondrial proteins have been shown to contribute to common metabolic diseases such as type 2 diabetes, insulin resistance, obesity, and cancers resulting from metabolic dysfunction (*2*–*4*). There is growing evidence from genetic and genome-wide association studies (GWAS) that genetic variation in mitochondrial DNA (mtDNA) contributes to these common metabolic diseases (*5*); however, there has been essentially no in vivo functional validation for these findings. Recently, a missense variant (rs11156878, Asn437Ser) was identified in the mitochondrial ribonuclease P subunit 3 (*MRPP3*) gene, which encodes an RNA binding protein suggested to be responsible for 22% of the variance in mitochondrial tRNA position 9 methylation in up to 19% of the population (*6*). This study predicted that the variant may have likely consequences on metabolism (*6*); however, this genetic association has not been functionally validated and its role in metabolism remains unknown.

The mitochondrial genome codes for 13 proteins that are all essential components of the electron transport chain and the adenosine triphosphate (ATP) synthase, which are responsible for energy production by oxidative phosphorylation (OXPHOS). Mutations in mtDNA most commonly lead to mitochondrial diseases and, in some instances, contribute to the onset and development of diabetes due to impaired insulin secretion (*7*, *8*), although the molecular mechanisms of these pathologies are unclear and are predominantly thought to involve OXPHOS dysfunction. Human mtDNA is circular and largely devoid of noncoding sequences, encoding 11 mRNAs, 22 transfer RNAs (tRNAs), and 2 ribosomal RNAs (rRNAs) that are transcribed as large polycistronic transcripts covering almost the entire length of each strand of the genome (*9*). The lack of introns in mtDNA genes has eliminated the requirement for splicing; instead, the tRNA genes, which are interspersed between mRNA and rRNA coding genes, enable recruitment of tRNA processing enzymes to produce the individual transcripts (*10*). Mitochondrial RNA processing involves cleavage at the 5′ end of tRNAs by ribonuclease (RNase) P (*11*, *12*) and cleavage of the 3′ tRNA ends by the mitochondrial RNase Z, encoded by the *ELAC2* gene (*13*). Impaired RNA processing has profound effects on mitochondrial and nuclear gene expression, protein synthesis, and, consequently, the assembly and function of the respiratory chain, causing premature death (*12*–*14*).

The mitochondrial RNase P is a proteinaceous complex, devoid of a catalytic RNA and composed of three proteins: mitochondrial RNase P protein 1 (MRPP1, also known as tRNA methyltransferase 10C homolog, TRMT10C), MRPP2 or HSD17B10 (hydroxysteroid 17-β dehydrogenase 10), and MRPP3 also known as the protein only RNase P catalytic subunit (PRORP) (*11*). Although MRPP3 has the catalytic RNA cleavage function, all three proteins are required for RNase P activity (*11*). Dysfunction of any component of the RNase P can

[1]Harry Perkins Institute of Medical Research, Nedlands, Western Australia 6009, Australia. [2]ARC Centre of Excellence in Synthetic Biology, QEII Medical Centre, Nedlands, Western Australia 6009, Australia. [3]Centre for Medical Research, The University of Western Australia, QEII Medical Centre, Nedlands, Western Australia 6009, Australia. [4]Max Planck Institute for Biology of Ageing, D-50931 Cologne, Germany. [5]Faculty of Health and Medical Sciences, Medical School, The Rural Clinical School of Western Australia, The University of Western Australia, Bunbury, Western Australia 6230, Australia. [6]Department of Anatomy and Embryology, Faculty of Medicine, Laboratory Animal Resource Center (LARC), and Transborder Medical Research Center, University of Tsukuba, 1-1-1 Tennodai, Tsukuba, Ibaraki 305-8575, Japan. [7]Dobney Hypertension Centre, Medical School, The University of Western Australia, Perth, Western Australia, Australia. [8]Australian National Phenome Centre, Centre for Computational and Systems Medicine, Health Futures Institute, Murdoch University, Harry Perkins Building, Perth, Western Australia 6150, Australia. [9]School of Human Sciences (Physiology), The University of Western Australia, Crawley, Western Australia 6009, Australia. [10]Victor Chang Cardiac Research Institute, Darlinghurst, Sydney, New South Wales 2010, Australia. [11]Curtin Medical School, Curtin University, Bentley, Western Australia 6102, Australia. [12]Curtin Health Innovation Research Institute, Curtin University, Bentley, Western Australia 6102, Australia. [13]Telethon Kids Institute, Northern Entrance, Perth Children's Hospital, 15 Hospital Avenue, Nedlands, Western Australia, Australia. [14]School of Molecular Sciences, The University of Western Australia, Crawley, Western Australia 6009, Australia.
*Corresponding author. Email: aleksandra.filipovska@uwa.edu.au

affect RNA processing with dire consequences for energy metabolism (*12*, *14*, *15*). This is evident from loss of, or mutations in, RNase P components that cause embryonic lethality in mice (*12*) or lead to severe multisystem disorders and premature death in humans by disruption of 5′ tRNA processing (*14*, *15*). In addition to facilitating tRNA processing within the RNase P complex, MRPP1 and MRPP2 have other roles in mitochondria. MRPP1 moonlights as a methyltransferase that modifies guanine or adenine at position 9 of mitochondrial tRNAs (*16*, *17*), and MRPP2 is a member of the short-chain dehydrogenase superfamily, required for branched chain amino acid (BCAA) and steroid hormone metabolism (*18*).

The influence of nuclear genetic variation on the mitochondrial transcriptome and how it can predispose to common metabolic disease has not been investigated by functional studies or using in vivo models previously. Therefore, we sought to investigate how the variant in the *MRPP3* gene affects the mitochondrial transcriptome and function. We used CRISPR-Cas9 genome editing to introduce the rs11156878 variant in the mouse *Mrpp3* gene and show that, on a high-fat diet (HFD), the mutation desensitizes pancreatic β cells by perturbing insulin secretion. Our work provides functional and mechanistic evidence for diet-specific effects of a common variant in the human population that may predispose to insulin resistance.

RESULTS

The *Mrpp3* variant causes insulin resistance in mice fed an HFD

The Asn437Ser variant predicted by GWAS to affect metabolic function and the mitochondrial epitranscriptome is present at variable frequencies in the human population, ranging from highest at 15 to 19% in European, followed by 6 to 11% in Asian, and lowest at 3 to 6% in African populations (gnomAD, 1000 Genomes Project; Fig. 1A). The asparagine at position 437 is conserved from humans to rodents (Fig. 1B). Atomic structures of the MRPP3 or PRORP enzyme revealed that it consists of a metallonuclease domain that carries out the endonuclease cleavage of tRNAs and a central linker and five tandem pentatricopeptide repeat (PPR) RNA binding domains, which are involved in tRNA binding (*19*–*21*). We used the atomic structures to model the Asn437Ser variant and show that it is located on the surface of the catalytic domain, well away from the catalytic site of MRPP3 (Fig. 1C). The Asn437Ser variant does not alter the local charge distribution on the surface of the catalytic domain (Fig. 1D).

We used CRISPR-Cas9 technology to knock in the equivalent Asn434Ser variant into the mouse *Mrpp3* gene to investigate its effect on metabolism, the mitochondrial transcriptome, and energy production compared to the wild-type *Mrpp3* gene. We bred the mice to produce homozygous variant *Mrpp3* mice (*N434S*) and homozygous wild-type *Mrpp3* mice (*wt*), and their genotypes were confirmed by Sanger sequencing (Fig. 1E). The mouse missense mutation was in an identical amino acid as in the human *MRPP3* gene and in a highly conserved region of MRPP3 that did not affect its abundance compared to the wild-type MRPP3 (fig. S1A). To understand the role of the Asn434Ser change in metabolism, we fed male *wt* mice and *N434S* littermates either a normal chow diet (NCD) or an HFD for 14 weeks. The *N434S* mice had a leaner phenotype with a lower body weight compared to the *wt* littermates on the NCD, but there was no difference in the body weight between the two genotypes on the HFD (Fig. 1F and fig. S1B). Glucose tolerance testing (GTT) revealed that the *N434S* mice were mildly glucose intolerant on both diets, compared to the *wt* control mice (Fig. 1G). Insulin tolerance testing (ITT) showed that the *N434S* mice fed on the HFD were desensitized to insulin compared to the *wt* mice (Fig. 1H). These findings indicate that the Asn434Ser variant may predispose to insulin resistance on an HFD.

An HFD in the *N434S* mice lowers circulating insulin levels, increases pancreatic islet size, and results in liver steatosis

The diet-specific effects of the *N434S* variant on insulin tolerance prompted us to investigate the pancreas because of its major role in glucose-stimulated insulin secretion and its target organs: the liver, skeletal muscle, and adipose tissue by hematoxylin and eosin (H&E) staining (Fig. 2 and fig. S2A). The pancreata and livers had the most obvious morphological changes in the *N434S* mice compared to the *wt* mice (Fig. 2). In the NCD-fed *N434S* mice, the pancreata had minor patches of early onset acini necrosis (Fig. 2A), whereas pancreata of the HFD-fed *N434S* mice showed severe loss of acini structure, acute necrosis likely due to the enzyme release of the acini, and larger islets of Langerhans compared to *wt* mice (Fig. 2A). The HFD-fed *wt* mice had low levels of necrosis, but the general tissue structure was unaffected and the acini had normal appearance (Fig. 2A). Pancreatic islet hyperplasia was consistent with reduced circulating insulin levels in the *N434S* mice that were fed an HFD compared to *wt* mice (Fig. 2B) and consistent with previous findings that larger islets of Langerhans are associated with lower insulin secretion (*22*). There were no major differences between the livers of the NCD-fed *N434S* and *wt* mice; however, H&E and Oil Red O staining revealed greater accumulation of lipid droplets in the livers of *N434S* mice fed an HFD, compared to *wt* mice on the same diet, indicating the presence of liver steatosis (Fig. 2C). Ectopic lipid storage in nonadipose tissue such as the liver has been identified in insulin resistance (*23*) and is consistent with the mild insulin resistance of the *N434S* mice on the HFD. In the skeletal muscle from *N434S* mice compared to the *wt* mice fed on an NCD, there was a slight increase in endomysial connective tissue and a mild presence of necrotic fibers, while on the HFD, there were some centralized nuclei in the skeletal muscle *N434S* mice compared to the *wt* mice (fig. S2A). There were signs of inflammation in the white adipose tissue of *N434S* mice compared to the *wt* mice fed on an NCD, while the HFD resulted in increased adipocyte size in the *N434S* mice compared to the *wt* mice (fig. S2B).

Circulating levels of albumin were reduced in the *N434S* mice fed on an NCD but were increased in the *N434S* mice on the HFD compared to their respective *wt* littermates (Fig. 2D). The marker of liver steatosis, alanine amino transferase (ALT), was significantly increased in the HFD-fed *N434S* mice compared to controls, further validating the Oil Red O staining findings. There were no differences in the high-density lipoprotein (HDL) and triacylglycerol (TAG) levels between the *N434S* and *wt* mice on either diet; however, cholesterol and low-density lipoprotein (LDL) levels were reduced in the *N434S* on the NCD and increased in the variant mice on the HFD (Fig. 2D), consistent with the predisposition of the *N434S* variant to insulin resistance on an HFD. Next, we measured the levels of circulating short-chain fatty acids (SCFA) in the serum, produced by the gut microbiota that have been used as markers of metabolic changes (*24*–*26*). The levels of the three SCFA were not different between the *N434S* and *wt* mice on an NCD (Fig. 2E). However, the levels of butyrate, shown to protect from diet-induced obesity and metabolic disorders (*24*, *25*), were significantly decreased, and acetate levels were increased

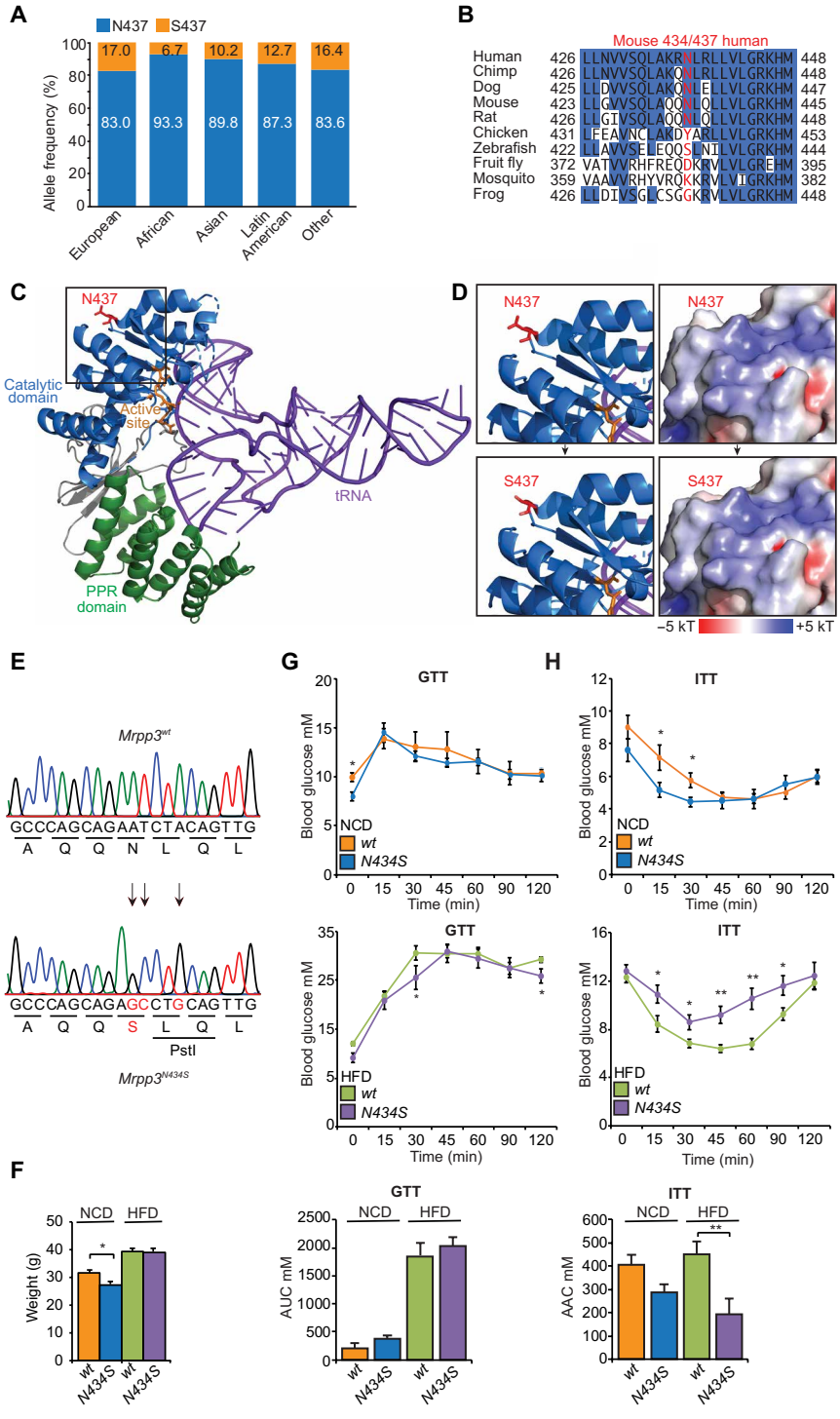

Fig. 1. The *N434S* mice develop insulin resistance when fed on a HFD. (**A**) Frequencies of the MRPP3 N437S single-nucleotide polymorphism (chr14:35266761 A>G, GRCh38.p12)(rs11156878) across different human populations. (**B**) Conservation of the MRPP3 protein sequence surrounding the N437S variant amino acid (red) is highlighted with residues identical to those in human sequence boxed in blue. (**C**) The location of N437 (red) is shown within the modeled structure of the human MRPP3 enzyme in complex with a tRNA substrate. The catalytic domain of MRPP3 is shown in blue, its four active site aspartates in orange, the PPR domain in green, and the bound tRNA in purple. (**D**) Close-up views of the N437 residue or N437S variant of MRPP3. The surface charge distribution is colored according to the local electrostatic potential (blue, +5 kT; red, −5 kT). (**E**) The N434S mutation in the *Mrpp3* gene was confirmed by Sanger sequencing of PCR amplicons from homozygous *N434S* and *wt* littermates. (**F**) Body weight of NCD and HFD-fed *wt* and *N434S* mice measured at 20 weeks of age. (**G**) Glucose tolerance tests (GTT) and (**H**) insulin tolerance tests (ITT) were carried out at 12 and 13 weeks of NCD or HFD, respectively. Quantitative values are area under the curve (AUC) for GTT or area above the curve (AAC) for ITT ± SEM **P* < 0.05 and ***P* < 0.01, Student's *t* test.

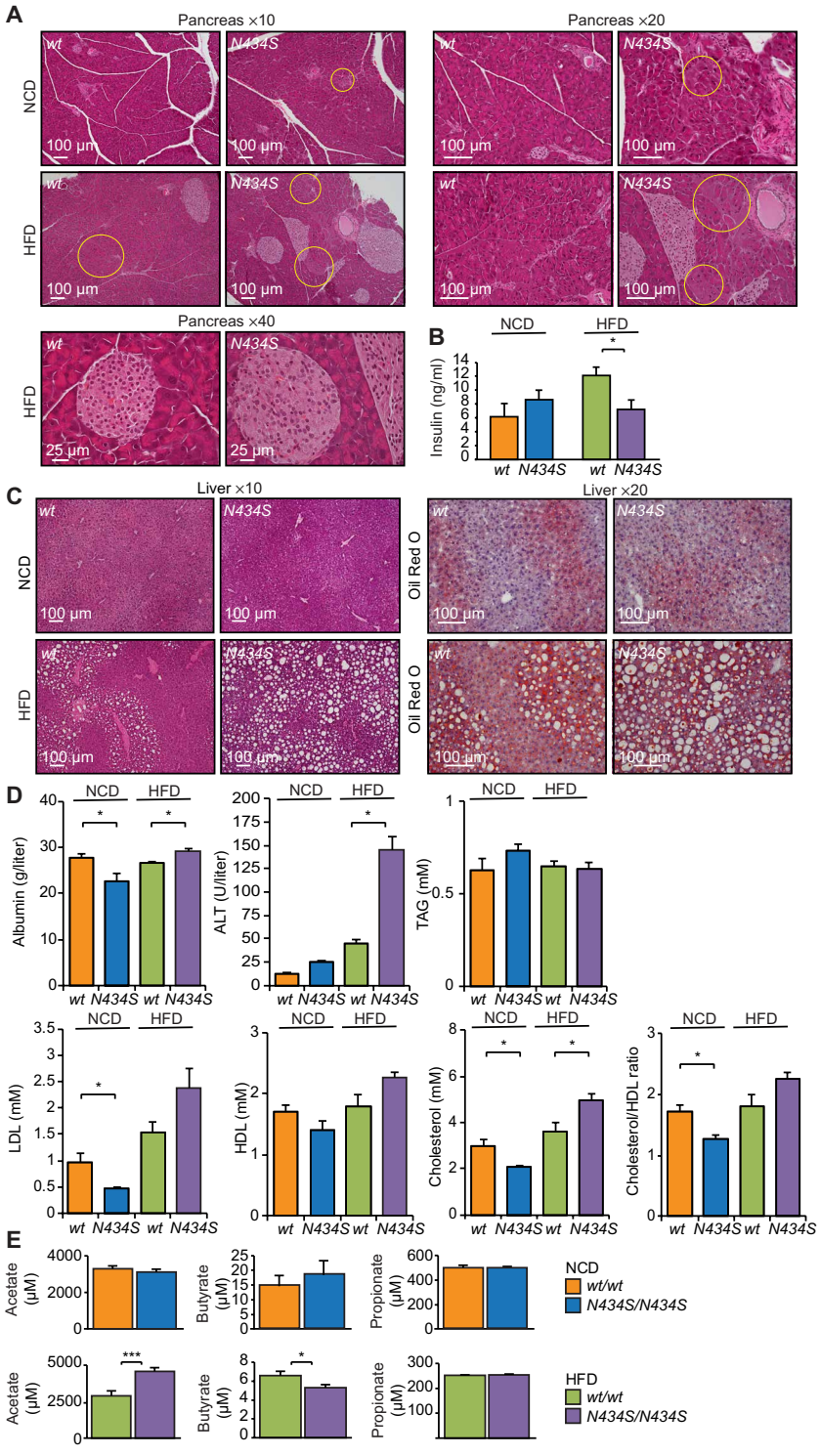

Fig. 2. The *N434S* variant leads to reduced circulating insulin and hepatosteatosis in HFD-fed mice. (**A**) H&E staining of pancreata from 20-week-old mice fed NCD show enzymatic necrosis of the acinar cells (yellow circles) in the *N434S* mice. Sections were visualized at ×10 (left), ×20 (right), or ×40 magnification (bottom). Scale bars, 100 and 25 μm. (**B**) Circulating insulin levels were measured in serum obtained from fasted 20-week-old *N434S* and *wt* ($n = 4$) mice fed either a NCD or a HFD. (**C**) H&E staining of liver sections from 20-week-old *wt* and *N434S* mice fed a NCD and a HFD (left) and Oil Red O staining (right). Magnification is ×10 or ×20. Scale bars, 100 μm. (**D**) Sera of 20-week-old *wt* and *N434S* mice fed a NCD or a HFD ($n = 4$) were analyzed for circulating albumin, ALT, TAGs, LDL, HDL, and cholesterol levels. (**E**) Sera of 20-week-old *wt* and *N434S* mice fed a NCD or a HFD ($n = 9$) were analyzed for short-chain fatty acids (SCFA) levels: acetate, butyrate, and propionate. Values are means ± SEM $^{*}P < 0.05$ and $^{***}P < 0.001$, Student's *t* test.

in the *N434S* mice compared to controls when they were fed an HFD (Fig. 2E), where previously increased acetate levels have been shown to induce metabolic syndrome (*26*). This is consistent with all the findings that the *N434S* variant reduces β cell sensitivity induced by an HFD and adversely affects gut microbiota.

We investigated the activation of the cellular insulin signaling pathway by immunoblotting against the serine/threonine protein kinase Akt and its activated form, phospho-Akt, either in basal conditions or following terminal insulin treatment. We found that both under basal conditions and after insulin treatment, Akt phosphorylation was not altered in the livers of the *N434S* and *wt* mice on either diets (Fig. 3, A and B), suggesting that insulin resistance did not involve changes in Akt signaling in the liver. In the pancreata, under basal conditions, Akt phosphorylation was increased in the *N434S* mice on NCD, compared to *wt* mice. However, on the HFD, the phosphorylation of Akt in the *N434S* mice was comparable to the *wt* mice (Fig. 3A). Insulin stimulation reduced Akt phosphorylation in the *N434S* mice fed a NCD, possibly as a compensatory response, and the levels of phospho-Akt were similar between the *N434S* and *wt* mice fed a HFD (Fig. 3B). There were no differences in the levels of the glucose transporter GLUT2, which can be activated following insulin stimulation, in the livers or pancreata of the *N434S* and *wt* mice on either diet (Fig. 3C). This indicated that impaired glucose uptake in the liver and by pancreatic β cells is not the cause of insulin resistance in the *N434S* mice. Because increased Akt phosphorylation in the pancreata *N434S* mice may affect mechanistic target of rapamycin (mTOR) activation via phosphorylation of S6, we used immunoblotting and found that on a NCD, S6 phosphorylation was increased in the *N434S* mice compared to controls (Fig. 3D). However, on an HFD, S6 phosphorylation was significantly reduced in *N434S* mice (Fig. 3D), suggesting that insulin resistance resulted in down-regulation of the mTOR pathway via S6. In the skeletal muscle from *N434S* mice fed an HFD, Akt phosphorylation was significantly reduced along with the levels of GLUT4 compared to control mice (fig. S2C), and this was due to reduced glucose uptake (fig. S2D), which resulted in insulin resistance in the *N434S* mice.

Next, we investigated the effects on mitochondrial respiration and whether lipid accumulation in the liver was associated with a preference toward the use of glucose over fatty acids as substrates for energy production and in response to the different diets. We measured both oxygen consumption via the S-linked pathway by stimulating respiration using succinate and β-oxidation rates via the F-linked pathway using palmitoylcarnitine in isolated liver mitochondria from *N434S* and *wt* mice. Oxygen consumption via the S-linked pathway was not affected in the NCD-fed *N434S* mice compared to controls (fig. S3A). However, there was a reduction in the oxygen consumption in the Leak (L) and OXPHOS (P) states in the F-linked pathway (fig. S3B), indicating that fatty acid oxidation in the *N434S* mice was reduced on the NCD. The HFD caused a significant increase in respiration via the S-linked pathway in the *N434S* mice (fig. S3C), whereas fatty acid oxidation was not significantly affected in the *wt* and *N434S* mice, but there was mild uncoupling of OXPHOS in the *N434S* mice on the HFD (fig. S3D).

To determine whether the changes in the NCD liver S-linked pathway were driven by a decreased influx of long-chain fatty acids (LCFAs) inside mitochondria, we analyzed the levels of the carnitine palitoyltransferase complex (CPT), responsible for the transfer of LCFAs inside mitochondria, and specifically its subunit carnitine palmitoyltransferase II (CPTII). The levels of CPTII were not altered in the livers of the *wt* and *N434S* mice on either diet, suggesting that only the use but not the uptake of fatty acids in mitochondria was affected by the variant (fig. S3E). Together with the oxygen consumption findings, we show that liver mitochondria of *N434S* mice prefer to use glucose over fatty acids for ATP production, which likely contributes to the development of liver steatosis.

Insulin resistance in the *N434S* mice is not the result of mitochondrial posttranscriptional RNA modification

To understand the metabolic differences between the *wt* and *N434S* mice, we investigated how the variant affects the molecular role of MRPP3. RNA sequencing of pancreatic islet cells revealed that the MRPP3 variant did not affect mitochondrial RNA processing when the mice were fed on a NCD (Fig. 4A). However, we observed small increases in unprocessed tRNA junctions across the entire mitochondrial transcriptome in the *N434S* mice compared to controls fed on an HFD (Fig. 4A). We used quantitative reverse transcription polymerase chain reaction (qRT-PCR) to confirm that on the NCD, the variant did not affect RNA processing, but on the HFD, there were increases in the unprocessed mitochondrial tRNA junctions in the pancreata (Fig. 4B). Mitochondrial RNA processing was not significantly affected in the livers of the *N434S* and *wt* mice on either diet (fig. S4A), but there were small reductions in the stability of some mature mtRNAs (fig. S4B). This indicated that the variant has a greater effect in the pancreas that is consistent with the most significant changes found in the pancreas including increased islet size, reduced insulin levels, and insulin resistance.

We used small RNA sequencing to determine the effects of the *N434S* variant on the modification of position 9 of mitochondrial tRNAs by measuring the increased sequencing error rate at this position in pancreatic islet cells from *wt* and *N434S* mice (Fig. 4C). We found that the MRPP3 variant does not affect the methylation status of mitochondrial tRNAs at position 9, and it does not affect the stability and abundance of mt-tRNAs (Fig. 4, C and D). Therefore, the variant does not affect the posttranscriptional modification of mt-tRNAs (*6*), which is entirely consistent with the role of the MRPP3 enzyme in tRNA cleavage and not tRNA modification (*17*).

We investigated the steady-state levels of OXPHOS proteins in the pancreata and livers of the *wt* and *N434S* mice on both diets by immunoblotting. There were no changes in the levels of OXPHOS proteins in the livers of the *wt* and *N434S* mice on both diets (fig. S4C), consistent with the minimal effects on mtRNAs. Similarly, the OXPHOS protein levels were not different in the pancreata of the *wt* and *N434S* mice on either diet, with the exception of the increased levels of ATP5A subunit of complex V in the *N434S* mice fed an HFD (Fig. 4E). In addition, there were no changes between the *wt* and *N434S* mice on either diet in the heart (fig. S5A) or skeletal muscle (fig. S6A) of the OXPHOS proteins. There were no changes in MRPP2, lipid and glucose import transporters in the hearts (fig. S5B), and skeletal muscle of the variant and control mice (fig. S6, B and C), further indicating that the variant influences predominantly pancreatic function but not its target organs. Furthermore, these data indicate that the *N434S* variant does not affect the catalytic function of MRPP3; thereby, it does not compromise mitochondrial RNA processing sufficiently to affect normal OXPHOS levels and function. Therefore, the *N434S* variant does not cause insulin resistance via changes in OXPHOS in contrast to what has been previously observed when mitochondrial gene expression has been compromised (*27*, *28*).

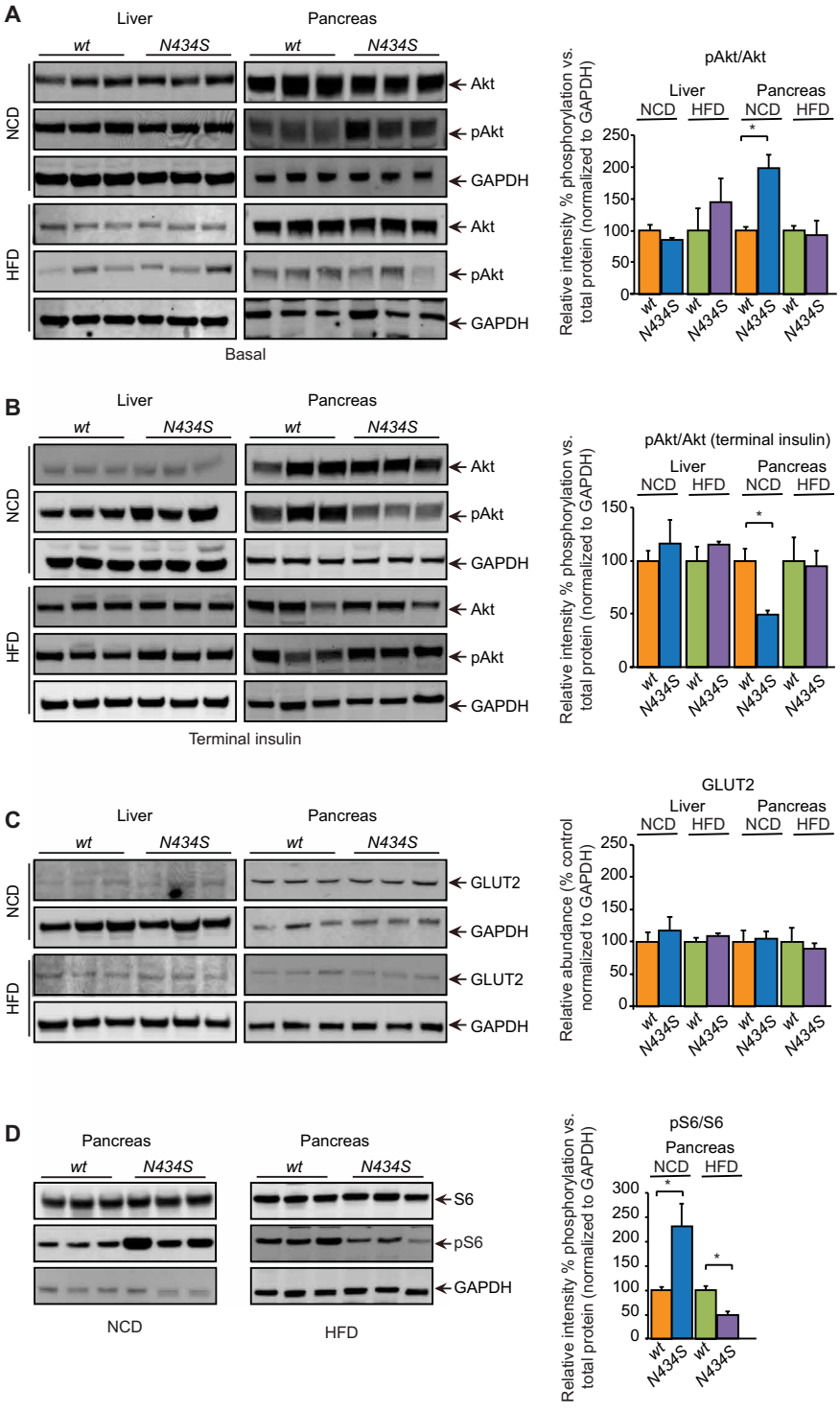

Fig. 3. Changes in Akt and mTOR signaling but not the expression of glucose transporters in *Mrpp3-N434S* mice. Liver and pancreas whole tissue lysates (30 μg) from 20-week-old *N434S* mice and *wt* mice fed a NCD or a HFD were immunoblotted against antibodies to investigate the endogenous levels of Akt and its phosphorylated form (Ser^{473}) under basal conditions (**A**) and following insulin exposure (terminal insulin) (**B**), where the mice were injected with insulin (1 U/kg) and euthanized after 5 min before the tissue was collected. Glyceraldehyde phosphate dehydrogenase (GAPDH) was used as a loading control. (**C**) Immunoblotting against the glucose transporter proteins (GLUT2) in livers and pancreata lysates (30 μg) from 20-week-old *N434S* mice and *wt* mice fed a NCD or a HFD. GAPDH was used as a loading control. (**D**) Immunoblotting against the S6 and phospho-S6 in pancreata lysates (30 μg) from 20-week-old *N434S* mice and *wt* mice fed a NCD or a HFD. GAPDH was used as a loading control. Relative abundance of proteins was measured using Image Studio Lite and normalized to GAPDH. The data are representative of results obtained from at least six mice from each genotype and diet. Error bars $^*P < 0.05$, Student's *t* test.

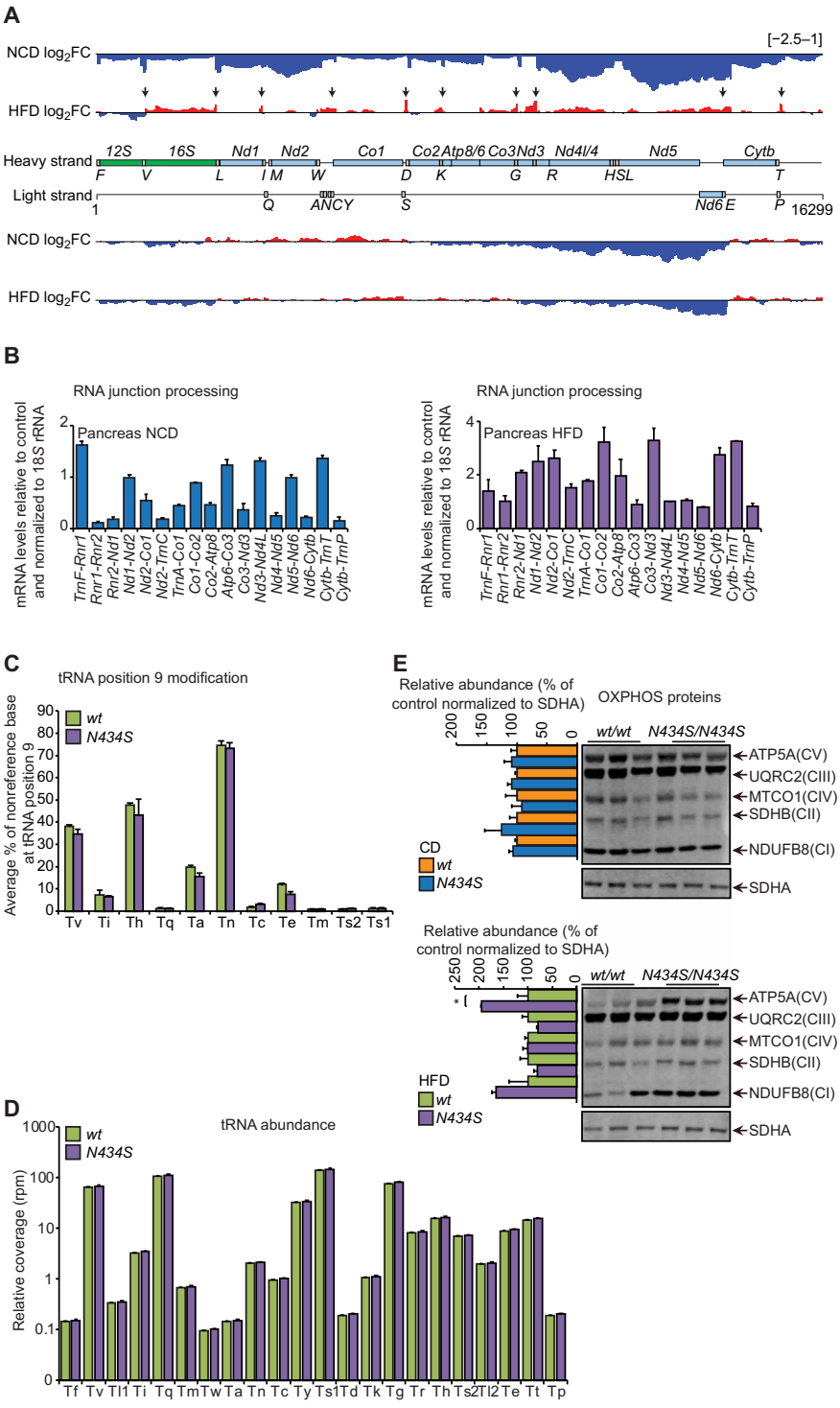

Fig. 4. Mitochondrial RNA processing and posttranslational tRNA modification are not functionally affected by the *N434S* variant. (**A**) A complete map of mtRNA abundance and mean $\log_2$ fold change (FC) [(KOmean/Ctrlmean)] determined by RNA sequencing coverage in pancreatic islets from 20-week-old *N434S* and *wt* mice fed a NCD or HFD ($n = 3$). Increases are shown in red and decreases in blue. The $\log_2$ fold changes range from −2.5 to 1. (**B**) qRT-PCR was used to measure mitochondrial RNA junctions in pancreata from 20-week-old *N434S* and *wt* mice either fed a NCD or a HFD ($n = 3$). Data were normalized to 18*S* rRNA. Error bars are means ± SEM. (**C**) Relative rate of nonreference bases, indicative of modification, at the ninth mt-tRNA position relative to a nonreference tRNA position and (**D**) relative tRNA abundance, determined by small RNA sequencing in pancreatic islets from 20-week-old *N434S* and *wt* mice fed a HFD ($n = 3$). Data were normalized to total library size. (**E**) Pancreatic mitochondrial proteins (30 μg) were isolated from 20-week-old *N434S* mice and *wt* mice fed a NCD or a HFD and immunoblotted against OXPHOS proteins and normalized to SDHA.

The MRPP3 *N434S* variant has reduced association with MRPP2 and the cation transporter LETM1

To identify proteins that are differentially associated with either the wild-type or variant form of MRPP3, we performed a proximity-biotinylation assay (BioID) followed by affinity purification and mass spectrometry. Before proceeding with the assay, we successfully assessed in 143B cells that the hemagglutinin (HA) tag fused to MRPP3 and MRPP3-N434S variant protein did not interfere with the normal expression and localization of the protein inside mitochondria (fig. S7). BioID identified that the MRPP3 variant caused reduced association with the leucine zipper and EF-hand containing transmembrane protein 1 (LETM1) (Fig. 5A). To validate the BioID result and explore the interactions between LETM1 with the RNase P complex subunits, we used a bimolecular fluorescence complementation assay (*29*) where LETM1 was fused to the N-terminal portion of Venus and each of the RNase P protein subunits, MRPP1, MRPP2, or MRPP3, was fused to the C terminus of Venus. Cells transfected with both N-terminal and C-terminal fusions of the proteins that interact with each other would enable the formation of a fluorescent Venus protein that was detected by fluorescence flow cytometry. We show that the glutathione *S*-transferase 1 (GST1) in combination with MRPP1 as a control was not fluorescent above background (Fig. 5B). We found that the direct association of both the *wt* and *N434S* MRPP3 with LETM1 is similar and relatively weak, and there is no association of LETM1 with MRPP1 (Fig. 5B). In contrast, we identified that there is a very strong association of LETM1 with MRPP2, and it is likely that through this interaction that the RNase P complex associates with LETM1 (Fig. 5B). To test this hypothesis, we investigated the association of the *wt* and *N434S* MRPP3 with the other two RNase P subunits (Fig. 5C). We show that the interaction of the *N434S* MRPP3 with MRPP2 is reduced compared to the interaction between the *wt* MRPP3 with MRPP2 (Fig. 5C). In contrast, the interactions between MRPP1 and the *wt* or *N434S* variant were comparable, albeit weaker compared to the MRPP2-MRPP3 association. To confirm this result, we used immunoprecipitation of HA-tagged *wt* or *N434S* MRPP3 and identified that the association of the MRPP3 variant protein was reduced with LETM1 and MRPP2 in NIH-3T3 cells (Fig. 5D). These three independent methods indicate that the RNase P complex associates with LETM1 and that the *N434S* variant reduces the association of MRPP3 with MRPP2, which, in turn, associates with LETM1.

To evaluate the effects of the *wt* and *N434S* MRPP3 on levels of LETM1 and MRPP2, we used immunoblotting and found that both LETM1 and MRPP2 levels were reduced in the pancreata of *N434S* mice fed a NCD, and both were increased in the HFD-fed *N434S* mice compared to their respective controls (Fig. 5E and fig. S8A). Given the strong interaction between LETM1 and MRPP2, our findings suggest that the levels of these proteins are dependent on or coregulated with each other as they associate closely together in the pancreas. In the livers of the *N434S* mice, the levels of LETM1 and MRPP2 were not affected on the NCD; however, the levels of these proteins were reduced on the HFD (fig. S8B). We also investigated the levels of other mitochondrial RNA and DNA binding proteins that are required for mtRNA stability, such as leucine rich pentatricopeptide repeat containing protein (LRPPRC), or required for mtDNA stability, such as Mitochondrial transcription factor A (TFAM), and found that their levels were largely unaffected in the pancreata and livers of the *wt* and *N434S* mice on either diet (fig. S8, C and D), further confirming that the gene expression machinery in mitochondria is not affected by the variant. The levels of the mitochondrial calcium uniporter (MCU) were also not affected by the variant on either diet (fig. S8E), indicating that the general pathways for mitochondrial calcium homeostasis are maintained (*30*, *31*).

Because mitochondrial RNA processing was not affected, we investigated whether changes in MRPP2 levels affect its function in BCAA metabolism. We used mass spectrometry to quantify amino acid levels in pancreata and sera from *wt* and *N434S* mice on both diets (Fig. 5, F and G, and fig. S9). We found significant reduction of BCAA in both pancreata and sera from the HFD-fed *N434S* mice (Fig. 5, F and G), particularly isoleucine, where MRPP2 is elevated and has a direct role in its degradation (*32*). The reduction of BCAA in the HFD-fed *N434S* mice could also be a consequence of reduced mTOR activity.

The MRPP3 variant impairs calcium availability required for glucose-stimulated insulin release on an HFD

LETM1 is a mitochondrial cation transporter that has been shown to affect calcium and potassium levels (*33*–*36*). Changes in cytosolic calcium levels play an essential role in pancreatic β cell function because they trigger the exocytosis of insulin granules (*31*, *37*). Because the *N434S* mice fed an HFD had reduced circulating insulin levels, we sought to investigate changes in calcium levels in response to an NCD or HFD that may affect insulin release. We measured calcium levels using Fura-2 in pancreatic islet cells isolated from *wt* and *N434S* mice fed an NCD and HFD under basal conditions and after glucose treatment to induce insulin release (Fig. 6A). Glucose stimulation increased calcium levels in the pancreatic islet cells of *wt* and *N434S* mice fed on an NCD required for insulin release, albeit this increase was significantly greater in the *N434S* mice, likely a consequence of an insulin hypersecretion during fasting in these mice (Fig. 6A). The calcium levels in response to glucose were significantly increased relative to basal levels in the pancreatic islet cells of *wt* and *N434S* mice fed an HFD; however, the calcium levels in the *N434S* mice fed an HFD and required for insulin secretion were markedly reduced compared to the NCD (Fig. 6A). We used Rhod-2 to measure mitochondrial calcium levels and found that they followed the changes in cytoplasmic calcium (Fig. 6, A and B). Mitochondrial calcium levels were increased in both basal and glucose-stimulated pancreatic islet cells from *N434S* mice compared to *wt* mice on an NCD (Fig. 6B). In contrast, mitochondrial calcium levels were reduced in response to glucose stimulation in the *N434S* mice compared to *wt* mice fed an HFD (Fig. 6B), consistent with reduced insulin sensitivity in the HFD-fed *N434S* mice. Because LETM1 has also been characterized as a potassium antiporter (*31*, *35*, *38*), we measured potassium levels in the serum of *wt* and *N434S* mice and show that there is significant reduction in circulating potassium levels in the *N434S* mice compared to controls on an HFD (Fig. 6C). We used JC-1 to measure the changes in the mitochondrial membrane potential in pancreatic islet cells and found that it was significantly elevated in the *N434S* mice fed an NCD (fig. S10A), possibly a consequence of reduced LETM1 levels and consequent imbalance in cation transport, that is subsequently equalized on the HFD as the LETM1 levels were increased.

To investigate whether changes in calcium affect insulin abundance, we measured insulin levels in the pancreata of *wt* and *N434S* mice on both diets and found that the *N434S* variant did not affect insulin production (Fig. 6D). This was further validated by fluorescent staining of pancreata for insulin and glucagon, which revealed

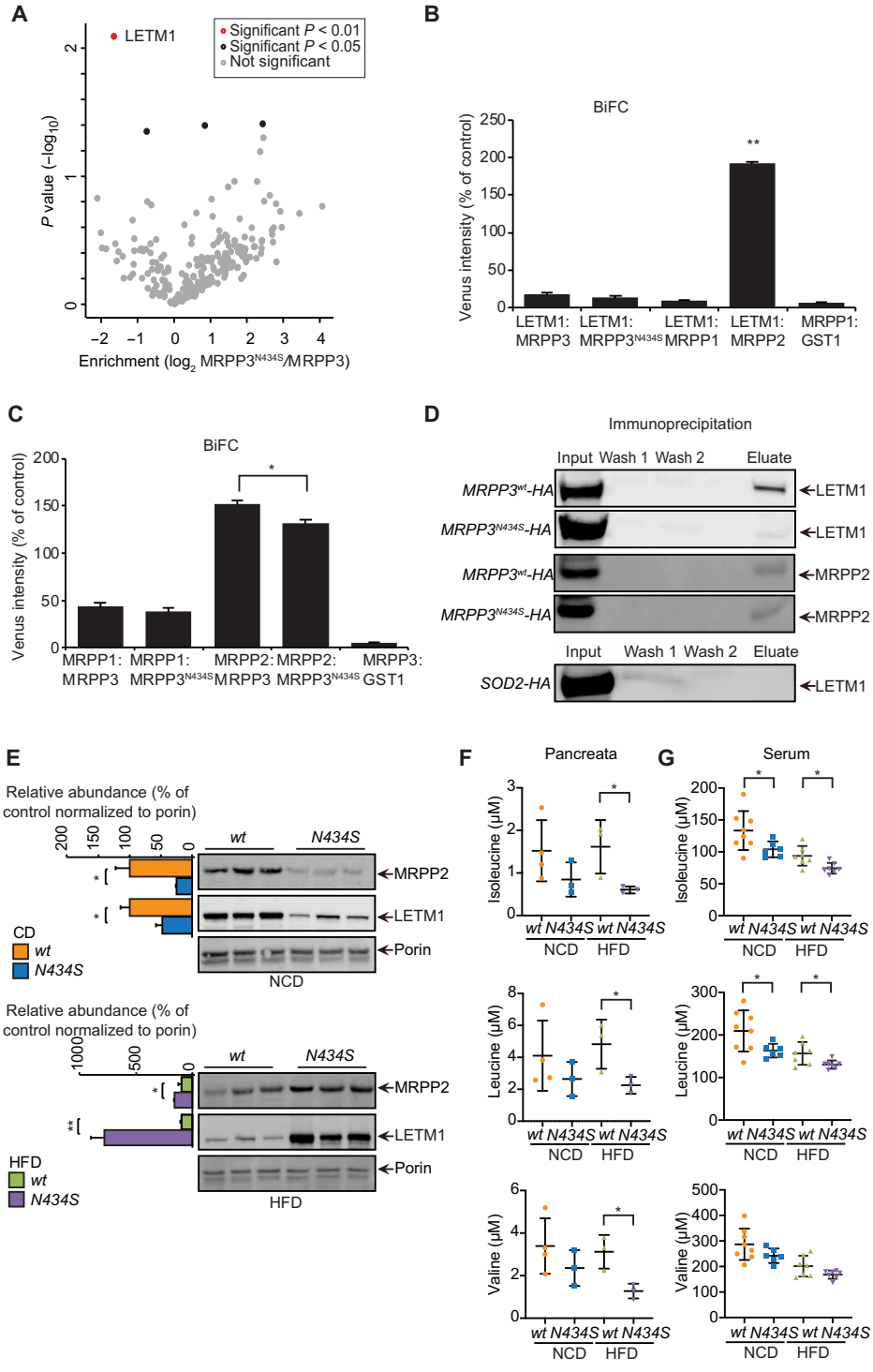

Fig. 5. The MRPP3 *N434S* variant reduces its association with LETM1 via MRPP2. (**A**) BioID of BirA*-tagged *wt* or *N434S* MRPP3 expressed in HeLa cells and the associated proteins were detected by mass spectrometry. Mitochondrial-targeted BirA* (mt-BirA*) was used as a control. (**B**) Average Venus intensities normalized to red fluorescent protein (RFP) intensity for interactions between LETM1 and the *wt* or *N434S* MRPP3, as well as MRPP1 and MRPP2 in NIH-3T3 cells determined by fluorescence-activated cell sorting. GST1 was used as a negative control. Data are shown as a percent change compared to the respective control. (**C**) Average Venus intensities normalized to RFP intensity comparing interactions between the *wt* and *N434S* MRPP3 with MRPP1 or MRPP2. GST1 was used as a negative control. (**D**) Immunoprecipitation of HA-tagged MRPP3 and MRPP3-N434S expressed in NIH-3T3 cells and immunoblots of the fractions from the immunoprecipitation against LETM1 and MRPP2. HA-tagged SOD2 was used as a control bait. (**E**) The levels of MRPP2 and LETM1 were measured by immunoblotting of pancreatic mitochondria and normalized to porin. Amino acid content was measured in pancreata (**F**) or serum (**G**) by mass spectrometry. All data are representative of results obtained from at least three experiments or three mice from 20-week-old *N434S* mice and *wt* mice fed an NCD or an HFD. Error bars are SEM $*P < 0.05$ and $**P < 0.01$, Student's *t* test.

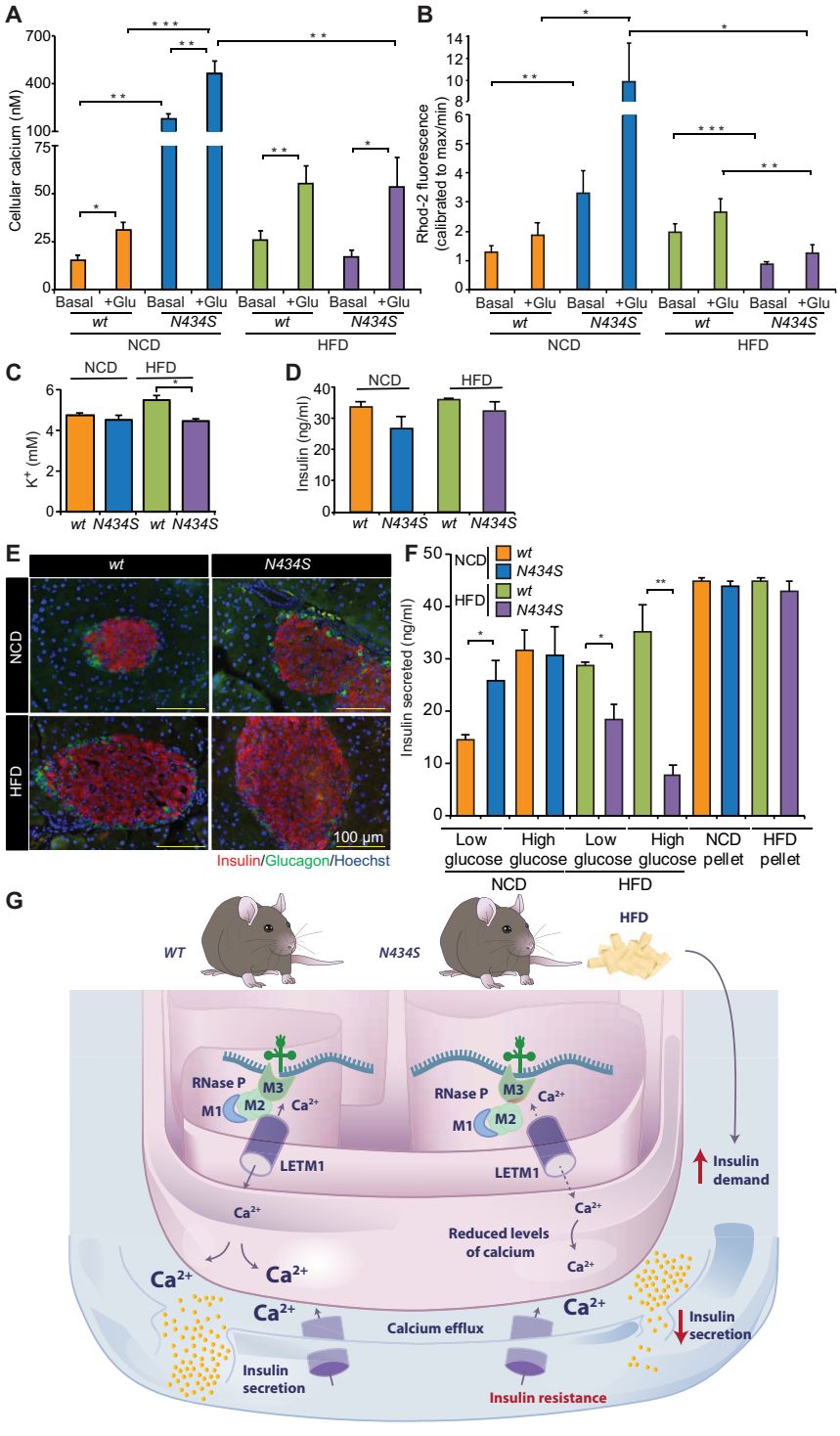

Fig. 6. The MRPP3 *N434S* variant results in reduced mitochondrial calcium and insulin secretion. Cellular (**A**) and mitochondrial (**B**) calcium levels were analyzed in isolated pancreatic β cells using Fura-2 or Rhod-2 fluorescent microscopy, respectively, under basal conditions and after exposure to glucose. (**C**) Potassium levels were measured in serum and (**D**) insulin levels were measured in pancreata by enzyme-linked immunosorbent assay (ELISA). (**E**) Insulin and glucagon levels were measured in pancreata by fluorescent immunohistochemistry. Hoechst staining was used to visualize the nuclei. (**F**) Glucose-stimulated insulin secretion was measured in pancreatic islet cells in the presence of low and high glucose, and total insulin levels were measured in the cell pellets as controls using an ELISA. All data are representative of results obtained from at least three mice from 20-week-old *N434S* mice and *wt* mice fed a NCD or a HFD. Error bars are SEM **P* < 0.05, ***P* < 0.01, and ****P* < 0.001, Student's *t* test. (**G**) Reduced RNase P association with LETM1 may affect calcium transport into mitochondria and the cellular calcium availability required for insulin secretion. The increased calorie intake from the HFD causes an increased requirement for insulin secretion, and the calcium levels are not sufficient to trigger increased insulin secretion that may eventually lead to insulin resistance.

that their levels were not affected by the *N434S* variant on either diet (Fig. 6E). We did not observe any inflammation markers in the livers or pancreata in the *wt* and *N434S* mice on both diets (fig. S10B), indicating that this did not play a role in insulin resistance or damage of the pancreas. The ratio of the autophagy marker LC3A/B isoforms (Light Chain 3 A/B isoforms I and II) was not different between in the *wt* and *N434S* mice fed on a NCD; however, on the HFD, the ratio between and longer and shorter isoform of LC3A/B was increased in the pancreata of *N434S* mice, indicative of autophagy (fig. S10C) that was consistent with increased necrosis identified by histology in these mice and the proposed role for MRPP3 in mitochondrial stress response (*39*).

Because insulin abundance was not affected, we investigated whether changes in calcium affected insulin release. We measured glucose-stimulated insulin release from the pancreatic islet cells from *wt* and *N434S* mice on either diet to determine whether the secretion of insulin was impaired. We found that the insulin secretion was perturbed in the *N434S* mice fed on an NCD compared to *wt* mice, consistent with their increased calcium levels and hypersecretion of insulin sensitivity (Fig. 6F). In contrast, the *N434S* mice fed on an HFD had significantly lower insulin secretion capacity compared to their respective controls (Fig. 6F), consistent with reduced calcium levels, lower circulating insulin levels, and insulin resistance. The cell pellets contained comparable levels of insulin, further indicating that the variant did not compromise insulin production. Therefore, our findings indicate that the MRPP3 variant leads to altered cellular calcium availability that contributes to decreased insulin secretion causing reduced β cell sensitivity to increased glucose levels and potential development of insulin resistance on a high-calorie diet that imposes a greater requirement for insulin (Fig. 6G).

DISCUSSION

Many variants in genes encoding mitochondrial proteins identified by GWAS have been suggested to alter metabolism; however, functional validation and mechanistic explanation of how they could affect metabolism for almost all of these have been lacking. Here, we have created a unique mouse model that functionally examines the role of single-nucleotide polymorphism in the nuclear encoded MRPP3 protein (the equivalent of the human missense variant *rs11156878*) on mitochondrial function and metabolism in vivo. We found that the *N434S* variant of the MRPP3 protein resulted in a leaner phenotype with lower fasting glucose. However, on an HFD, this polymorphism reduced insulin release from the pancreas and decreased insulin sensitivity, indicating that the *N434S* variant predisposes to metabolic dysfunction. The variant MRPP3 affected pancreatic function and the insulin-secreting pancreatic β cells most significantly, where, on a NCD, the *N434S* mice were able to mount a β cell response that counters insulin resistance, but under the additional stress of the HFD, this compensation failed. The downstream consequences of decreased pancreatic insulin secretion and consequent reduced circulating insulin levels resulted in increased lipid accumulation in the liver and reduced glucose uptake in skeletal muscle. Despite the role of MRPP3 in mitochondrial gene expression, the mutation did not affect OXPHOS biogenesis nor its function; instead, impaired insulin secretion was a consequence of compromised calcium release from mitochondria.

In the GWAS, the missense variant *rs11156878* was proposed to modulate mitochondrial RNA sequence variation and thereby potentially influence basal metabolism; however, this was not functionally investigated (*6*). This was inferred most likely because of the roles of MRPP3 and MRPP1 in the RNase P complex in mitochondrial RNA processing and tRNA modification (*11*, *12*), respectively. However, we found that *N434S* variant did not alter the MRPP3 catalytic function, and mitochondrial RNA processing was not markedly impaired. The posttranscriptional modification of the ninth position in mitochondrial tRNAs by the MRPP1 methyltransferase, which forms a complex with MRPP3 and MRPP2 in the RNase P complex, was also not affected. The lack of mitochondrial transcriptome changes in the *N434S* mice indicated that the metabolic dysfunction was not caused by changes in mitochondrial gene expression, consistent with the unaltered mitochondrial biogenesis in the mice. Although regulation of mitochondrial gene expression is important for energy production and its impaired function can lead to insulin resistance or metabolic disorders (*27*, *28*, *40*), the *N434S* variant in MRPP3 had an alternate mechanism that led to insulin resistance. We showed using three separate methods (BioID, immunoprecipitation, and bimolecular fluorescence complementation) that the RNase P component MRPP2 associates with the cation transporter LETM1, and this association is affected by the reduced interaction between MRPP2 and the MRPP3 *N434S* variant. The association between MRPP2 and LETM1 has been independently validated by recent high-throughput BioID analyses of mitochondrial protein interactions (*41*), and we found that the levels of these proteins are coregulated in vivo. The reduced association between MRPP2 and the MRPP3 *N434S* variant did not affect RNA processing particularly as part of their role in the RNase P complex, most likely because the variant is away from the active site of the enzyme. However, the altered association and levels of LETM1 and MRPP2 from the RNase P complex may contribute to decreased mitochondrial calcium and consequently affect intracellular calcium levels that are required for insulin secretion (*31*, *37*), in addition to the main mitochondrial calcium transporters.

LETM1 and its yeast ortholog have been shown to associate with mitochondrial ribosomes and affect mitochondrial protein synthesis (*42*, *43*), although the changes in LETM1 levels did not affect mitochondrial biogenesis in the *N434S* mice. Instead, we only identified changes in intracellular calcium and circulating potassium levels in the pancreatic islet cells of *N434S* mice, suggesting that its role in cation transport (*31*, *38*) was the contributing factor for insulin resistance. This is consistent with the requirement for LETM1 for mitochondrial calcium uptake and normal glucose metabolism (*33*, *34*, *36*). In addition, the *N434S* variant resulted in reduced potassium levels in vivo, suggesting that LETM1 may also have a role in mitochondrial K^+-H^+ exchange as it has been suggested previously [reviewed in (*38*)].

In the HFD-fed *N434S* mice, reduced insulin secretion correlated with reduced levels of BCAAs, including isoleucine, likely a consequence of increased levels of MRPP2, which has an irreversible role in isoleucine degradation (*32*). Recently, it has been suggested that in Wolf-Hirschhorn syndrome caused by LETM1 haploinsufficiency, low LETM1 levels stimulate consumption of ketone bodies by an unknown mechanism (*43*). It is possible that the association and coregulation of LETM1 with MRPP2 mediate changes in ketogenic or BCAA metabolism via its role in isoleucine oxidation. Loss-of-function mutations in MRPP2 cause severe neurological disorders through impaired BCAA metabolism and accumulation of toxic intermediates that cause mitochondrial dysfunction along with impaired mitochondrial RNA processing and OXPHOS biogenesis

(*15*, *32*). Furthermore, patients and animal models of impaired BCAA metabolism are susceptible to insulin resistance and type 2 diabetes [reviewed in (*44*)], features that are in common with our *N434S* mice where MRPP2 levels and BCAA were altered.

Under normal diet conditions, both *wt* and *N434S* mice produced comparable levels of insulin; however, the *N434S* variant conferred a predisposition to insulin resistance by the inability to effectively secrete insulin when there were excess nutrients and thereby long-term demand for insulin secretion. The increase of pancreatic islets in the HFD-fed *N434S* mice was likely a compensatory response to the increase in nutrients, because the *wt* mice were able to meet the insulin demand in response to excess nutrient availability, whereas insulin secretion was reduced in the *N434S* mice in response to reduced mitochondrial calcium. This indicated that mitochondrial calcium availability may be required to help insulin secretion when there is increased demand in the presence of excess nutrients, as this was compromised in the pancreatic β cells of the *N434S* mice on an HFD. The requirement for mitochondrial calcium for insulin secretion has been shown in pancreatic cells where knockdown of the Na^+-Ca^+ exchanger altered mitochondrial calcium transport, resulting in delayed glucose-stimulated insulin release without changes in ATP production (*45*). Recently, reduced mitochondrial calcium transport has been shown to reduce insulin secretion (*46*). Under normal conditions and basal insulin levels, cellular calcium levels were sufficient in the *N434S* variant mice to meet the demand for insulin secretion. However, an HFD elicited a long-term demand for insulin secretion that may consequently require increased release of calcium. The mitochondrial calcium levels in the *N434S* mice may be affected by the impaired interactions with LETM1, reducing the cells' ability to mobilize calcium to stimulate insulin release, ultimately resulting in decreased circulating levels of insulin, reduced β cell sensitivity to insulin, and accumulation of lipids in the liver.

The acquisition of variants in the human genome is essential for adaptation to diverse nutritional availabilities and requirements. Extreme habitats like the Artic, for example, led to the selection in the Inuit population of a variant in the mitochondrial carnitine palmitoyltransferase protein (CPT1A), because this provides a selective advantage in the metabolism of a diet rich in fat, typical of this indigenous population (*47*). It is currently not clear why the *rs11156878* variant in MRPP3 has been selected in as high as 19% of the population, it may be that it could provide an advantage by up-regulating insulin secretion under normal diet conditions. However, this genetic variant predisposes to insulin resistance in a diet rich in fat (HFD) as mitochondria are unable to mobilize their stored calcium levels in the pancreas to increase insulin secretion. The mitochondrial Ca^{2+} uptake 1 and MCU proteins are the main regulators of mitochondrial calcium uptake, and their levels are not altered in the mutant mice on either diet, indicating that the normal mode of insulin secretion is consistent with previous findings (*30*, *31*). Here, we are not challenging this model but merely suggest that LETM1, as it has been suggested before (*33*), may contribute to fine-tuning the release of calcium when challenged with an HFD.

Our study provides functional evidence and molecular mechanisms of how a common genetic variant found predominantly in European populations can affect cation transport and predispose to reduced insulin sensitivity on a high-calorie diet. This discovery could help to manage the nutrition of a significant number of individuals within human populations to prevent or delay the onset of insulin resistance and potential development of type 2 diabetes.

MATERIALS AND METHODS

MRPP3 variant analyses

Aggregate allele frequencies were obtained from the National Center for Biotechnology Information (NCBI) database of Genotypes and Phenotypes from the Allele Frequency Aggregator project (build 154, released 21 April 2020). Protein sequences from diverse species used were obtained from GenBank at NCBI (human, *Homo sapiens*, NP_055487.2; chimp, *Pan troglodytes*, XP_009425955.1; dog, *Canis lupus familiaris*, XP_547772.2; mouse, *Mus musculus*, NP_079649.1; rat, *Rattus norvegicus*, NP_001100200.1; chicken, *Gallus gallus*, XP_421241.2; zebrafish, *Danio rerio*, XP_683289.3; fruit fly, *Drosophila melanogaster*, NP_001245549.1; mosquito, *Anopheles gambiae*, XP_003435980.1; frog, *Xenopus tropicalis*, XP_002935379.1), and the alignment was produced using Clustal Omega.

The MRPP3 structure was modeled in PyMOL (Schrödinger) by aligning a human MRPP3 structure (PDB ID: 4XGL) to a structure of an engineered variant of the PPR domain of the *Arabidopsis thaliana* MRPP3 homolog (PRORP1) in complex with yeast $tRNA^{Phe}$ (PDB ID: 6LVR) using the CE algorithm to provide a final model of the human MRPP3 protein in complex with tRNA. The local electrostatic potential was modeled using the Adaptive Poisson-Boltzmann Solver program and visualized using PyMOL (Schrödinger).

Animals and housing

Heterozygous *Mrpp3 N434S* transgenic mice on a C57BL/6 N background were generated by the Monash Genome Modification Platform (MGMP) and the Australian Phenomics Network (APN). The N434S mutation was introduced into the *Mrpp3* gene by CRISPR-mediated homology-dependent repair using a single-stranded DNA oligo nucleotide donor containing an AAT → AGC codon change. A silent CTA → CTG change was introduced into the neighboring leucine codon to enable restriction fragment length polymorphism–based genotyping of the mutant mice. Male age- and littermate-matched wild-type (*wt*) and homozygous mutant mice (*N434S*) were housed in standard cages (45 cm by 29 cm by 12 cm) under a 12-hour light/dark schedule (lights on 7:00 a.m. to 7:00 p.m.) in controlled environmental conditions of 22° + 2°C and 50 + 10% relative humidity. NCD and water were provided ad libitum. HFD feed was provided ad libitum for 14 weeks. The feed was provided by Rat and Mouse Chow, Specialty Feeds, Glen Forrest, Western Australia. The study was approved by the Animal Ethics Committee of the University of Western Australia and performed in accordance with Principles of Laboratory Care (National Health and Medical Research Council Australian code for the care and use of animals for scientific purposes, eighth edition, 2013).

Metabolic studies

Six-week-old male mice were fed either a NCD or HFD for 14 weeks. During this time, their body weight and food intake were monitored weekly. Intraperitoneal GTT and ITT were performed in up to 10 mice of each genotype and diet after the mice were fasted for 5 hours. GTTs (1 g/kg) were performed at week 12, and ITTs (1 U/kg) were performed at week 13. Blood glucose levels were measured using a glucometer (Accu-Chek Informa II, Roche). Blood was sampled from the tail tips at 0, 15, 30, 45, 60, 90, and 120 min after glucose or insulin injection. The area under or above the curve was calculated using the trapezoidal rule using Excel software (Microsoft). Mice were humanely euthanized at 20 weeks of age after 14 weeks on their respective diets. Methoxyflurane was used to anesthetize the mice to perform cardiac puncture and collect blood. The mice were

subsequently euthanized by cervical dislocation, and tissues were collected. Tissues were snap-frozen in liquid nitrogen and stored at −80°C. Tissues for histological analysis were either fixed in formalin or frozen in optimal cutting temperature (OCT) embedding medium. For terminal insulin testing, 20-week-old mice were injected with insulin (1 U/kg) and euthanized by cervical dislocation 5 min after the injection, followed by tissue collection (snap freezing). SCFA profiling was performed as described previously (*48*) to measure the concentration of acetate, butyrate, and propionate as nanomoles per microliter of serum. Serum was analyzed by Pathwest Laboratory Medicine (Nedlands, WA, Australia) for levels of albumin, ALT, cholesterol, TAG, LDL, HDL, and potassium (K^+). Glucose uptake measurements were carried out in vitro with skeletal muscles isolated from 20-week-old HFD-fed control and mutant mice as described before (*49*). Skeletal muscles were incubated in "pregassed" (95% O_2 and 5% CO_2) Krebs-Henseleit-bicarbonate (KHB) buffer containing 0.01% bovine serum albumin (BSA), 2 mM pyruvate, and 8 mM mannitol for 30 min at 35°C. Muscles were then incubated for 30 min at 30°C in KHB with or without 50 nM insulin. Glucose transport was measured after a 16-min incubation at 30°C with 1 mM 2-deoxyglucose, 2-deoxy-D-[2, 6-^{3}H]-glucose (0.25 μCi/ml), and D-[^{1}4C]-mannitol in KHB (0.16 μCi/ml) with or without 50 nM insulin. Muscles were trimmed and frozen in liquid nitrogen and later weighed and incubated for 30 min at 65°C in 250 μl of 1 M NaOH, and at the end of the incubation, 250 μl of 1 M HCl was added to the dissolved muscle. Samples were centrifuged at 17,000*g* for 10 min, and radioactivity was determined by scintillation counting for dual-label dpm in the supernatants and muscles.

Enzyme-linked immunosorbent assay

Serum (fasting) was analyzed for circulating insulin levels using an insulin enzyme-linked immunosorbent assay (ELISA) kit (EZRMI-13K; Millipore, Australia). All tissue homogenates for ELISAs were prepared using a lysis buffer (10 mM Hepes, 3 mM $MgCl_2$, 14 mM KCl, 5% glycerol, and 0.2% IPEGAL) containing PhosSTOP Phosphatase Inhibitor Cocktail (Roche) and EDTA-free Complete protease inhibitor cocktail (Roche). Pancreas, liver, and skeletal muscle were analyzed for insulin levels (EZRMI-13K; Millipore). Data were analyzed using an online software program (https://www.assayfit.com/).

Histology

Fresh liver tissue was frozen in OCT medium and cut using a Cryostat (Leica, TP1020) to 10-μm thickness. All other tissues were fixed with 10% neutral buffered formalin for 24 hours, washed in phosphate-buffered saline (PBS), and stored in 70% ethanol before processing. Tissues were then embedded in paraffin, cut in 5- or 10-μm sections using a microtome, and transferred to positively charged slides. Slides were heated for 2 hours at 60°C and treated with xylene, xylene and ethanol (1:1), and decreasing concentrations of ethanol (100, 95, 80, and 60%) before they were washed and hydrated in distilled water. The H&E and Oil Red O staining were performed as described before (*50*). Coverslips were attached using DPX mounting media (Scharlau), and images were acquired using a Nikon Ti Eclipse inverted microscope using a Nikon 10× or 20× objective.

Respiration

Mitochondrial respiration was evaluated as O_2 consumption in isolated liver as previously described (*28*). Mitochondria were supplemented with substrates 10 mM glutamate/2 mM malate (Sigma-Aldrich) and 10 mM succinate/0.5 mM rotenone (Sigma-Aldrich), to measure adenosine diphosphate (ADP)–independent respiration activity (state 4). After addition of 1 mM ADP (Sigma-Aldrich), state 3 respiration activity was measured. Respiration was uncoupled by successive addition of carbonyl cyanide *p*-trifluoro-methoxyphenylhydrazone (FCCP) up to 3 mM to reach maximal respiration.

Fatty acid oxidation was measured from isolated liver mitochondria from mice fasted for 5 hours before sacrifice using the Oxygraph 2K respirometer (Oroboros Oxygraph-2K, Oroboros Instruments) as described in (*51*) and reviewed in (*52*). State 4 respiration was measured using 5 mM malate (Sigma-Aldrich) and 1 mM palmitoyl carnitine (Sigma-Aldrich), and state 3 respiration was measured using 1 mM K-ADP (Sigma-Aldrich) and 10 mM K-succinate (Sigma-Aldrich). Inhibitors used included 0.5 μM oligomycin (Sigma-Aldrich) and 2.5 μM antimycin. FCCP was used as a measure of uncoupling and maximal respiration rate in titrations up to 3 μM.

Tissue homogenate preparation

Tissue pieces (3 mm by 3 mm; liver and pancreas) were homogenized in 200 μl of Cell Extraction Buffer (100 mM tris, 2 mM Na_3VO_4, 100 mM NaCl, 1% Triton X-100, 1 mM EDTA, 10% glycerol, 1 mM EGTA, 0.1% SDS, 1 mM NaF, 0.5% deoxycholate, and 20 mM $Na_4P_2O_7$), pH 7.4, containing PhosSTOP Phosphatase Inhibitor Cocktail (Roche) and EDTA-free Complete protease inhibitor cocktail (Roche). The homogenates were prepared using a bead beater, and the homogenates were centrifuged at 9000*g* for 5 min at 4°C. The previous steps were repeated until a clear tissue homogenate was produced. The tissue homogenate protein concentration was quantified using the bicinchoninic acid (BCA) assay using BSA as a standard.

Mitochondrial isolation

Mitochondria were isolated from homogenized liver and pancreas and isolated by differential centrifugation as described previously (*12*, *53*). The mitochondrial protein concentration was quantified using the BCA assay using BSA as a standard.

Immunoblotting

Specific proteins were detected using the following rabbit monoclonal antibodies: phospho-SAPK/JNK (Thr^{183}/Tyr^{185}, 4668), SAPK/JNK (9252), phospho-Akt (Ser^{473}, 4060), Akt (9272), S6 ribosomal protein (2217S), phospho–S6 ribosomal protein (4856S), glyceraldehyde phosphate dehydrogenase (GAPDH) (2118), LC3A/B (12741) MCU (14997) (Cell Signaling Technologies), and MRPP3 (HPA020459) (Sigma-Prestige) diluted 1:1000; rabbit polyclonal antibodies: GLUT2 (54460) (Abcam) diluted 1:1000, GLUT4 (PA-1-1065) (Thermo Fisher Scientific), CPTII (OAAN00972) (Aviva System Biology) diluted 1:500, Letm1 (16024-1-AP) (Proteintech) diluted 1:1000, MRPP2 (HPA001432) (Sigma-Prestige) diluted 1:1000, LRPPRC (sc66844) (Santa Cruz Biotechnology) diluted 1:500, TFAM (ab131607) (Abcam) diluted 1:1000; mouse monoclonal antibodies: total OXPHOS Cocktail Antibody (ab110412), VDAC (ab14734), and SDHA (ab14715) (Abcam), diluted 1:1000. IRDye 800CW goat anti-rabbit immunoglobulin G (IgG) or IRDye 680LT goat anti-mouse IgG (LI-COR Biosciences) secondary antibodies were used, and the immunoblots were visualized using an Odyssey infrared imaging system (LI-COR Biosciences). Relative amount of protein was determined using the Image Studio Lite Software.

RNA isolation, Northern blotting, and qRT-PCR

The tissues were snap-frozen and stored at –80°C before RNA isolation, while pancreatic islets were isolated fresh using collagenase digestion as described below. RNA was isolated from tissues and pancreatic islets of Langerhans using the miRNeasy Mini kit (Qiagen) using an on-column RNase-free DNase digestion, and the isolated RNA (4 μg) was resolved on 1.2% agarose formaldehyde gels. Northern blotting was carried out as described previously (*13*) by transferring the RNA to 0.45 μm of Hybond-N^+ nitrocellulose membrane (GE Lifesciences) and hybridizing using biotinylated oligonucleotide probes as described before (*13*). Streptavidin-linked infrared-labeled antibody [diluted 1:10,000 in 3× SSC, 5% SDS, and 25 mM Na_2HPO_4 (pH 7.5)] was used to detect the signal and visualize the signal using the Odyssey Infrared Imaging System (LI-COR Biosciences). The QuantiTect Reverse Transcription Kit (Qiagen) was used to prepare complementary DNA (cDNA) that was used as a template for PCR. PCRs were performed using a Corbett Rotorgene 6000 using SensiMix SYBR mix (Bioline) and normalized to 18*S* rRNA.

RNA sequencing

RNA sequencing was performed on total pancreatic RNA isolated from three *wt* and three *N434S* mice fed on a NCD and a HFD. Sequencing was performed using the Illumina NovaSeq platform, according to the Illumina RNA-Seq protocol and as we have done previously (*13*). Sequenced reads were trimmed via TrimGalore v0.4.1 using cutadapt (*54*) v1.18 and FastQC (*55*) v0.11.8 in paired-end mode. Biologically independent reads (three from each genotype and treatment) were aligned against the mouse genome [GRCm38.p6 primary assembly (ftp://ftp.ebi.ac.uk/pub/databases/gencode/Gencode_mouse/release_M21/gencode.vM21.primary_assembly.annotation.gtf.gz; ftp://ftp.ebi.ac.uk/pub/databases/gencode/Gencode_mouse/release_M21/gencode.vM21.transcripts.fa.gz) masked for nuclear mitochondrial sequences] with STAR v2.7.0f (*56*) and the GENCODE vM23 gene annotation with a customized mitochondrial annotation. Full fragment length mitochondrial coverage profiles were generated with samtools v1.10 (*57*) and bedtools v2.26.0 (*58*) and normalized to total reads mapped to the mouse genome.

Small RNA sequencing

RNA sequencing was performed on total pancreatic RNA isolated from three *wt* and three *N434S* mice fed on a HFD. Sequencing was performed using the Illumina NovaSeq platform, according to the Illumina small RNA-Seq protocol and as we have done previously (*13*). Sequenced reads were trimmed via TrimGalore v0.6.5 using cutadapt (*54*) 0.18 and FastQC (*55*) v0.11.8 in paired-end mode with a minimum length of 18 nt. Biologically independent reads (three from each genotype and treatment) paired reads were merged using NGmerge v0.3 (*59*). Reads were aligned to the GRCm38.p6 genome sequence using STAR (*56*) and the GENCODE vM21 gene annotation (with customized mitochondrial annotations). Coverage was normalized to total mapped reads, and tRNA position 9 mismatch rates were calculated by extracting nucleotide frequencies from genomic BAM files with pysamstats [10] (--type variation_strand). tRNAs with an average raw read count of <50 across either sample group were filtered out.

BioID

MRPP3 and its N434S mutant were cloned into pcDNA3.1-MCS-BirA(R1186)-HA. The expression of MRPP3 and MRPP3-N434S variant and the mitochondrial localization of the proteins were checked by fluorescence cell microscopy as described in (*60*). The BioID analysis was carried out as described in (*61*). The data were results from three independent biological experiments, and all significantly enriched proteins are shown in black and red with 0.01% false discovery rate significance.

Immunoprecipitation

NIH-3T3 cells were transfected with *wt* or *N434S* MRPP3 with an HA tag fused to the C-terminal end and incubated for 72 hours. Cells were crossed linked in 2 mM dithiobis(succinimidyl propionate) (Life Technologies) in PBS for 30 min at room temperature followed by quenching in 50 mM glycine for 15 min. Cells were lysed in 260 mM sucrose, 100 mM KCl, 20 mM $MgCl_2$, 10 mM tris-HCl (pH 7.5), 1% digitonin, and complete EDTA-free protease inhibitor cocktail for 30 min at 4°C followed by sonication. Lysates were incubated with HA beads (Pierce) for 2 hours at 4°C. Beads were washed in digitonin wash buffer (same components as lysis buffer except with 0.1% digitonin), washed again in IGEPAL wash buffer (same components as lysis buffer except with 1% IGEPAL CA-630; Sigma-Aldrich), then eluted in 2× SDS–polyacrylamide gel electrophoresis (SDS-PAGE) sample buffer by heating at 95°C for 10 min. Five microliters of input samples, taken immediately after lysis, and the entire final elution samples were run on SDS-PAGE gels and analyzed by immunoblotting as described above.

Bimolecular fluorescence complementation

NIH-3T3 cells were transfected with separate plasmids encoding LETM1 with the VN fragment (amino acids 1 to 173 of Venus) attached to the C-terminal end and *wt* or *N434S* MRPP3 with the VC fragment (amino acids 174 to 239 of Venus) attached to the C-terminal end and mCherry red fluorescent protein (RFP) in a 2:2:1 ratio. Seventy-two hours after transfection, cells were treated with trypsin, resuspended in PBS + 2% fetal bovine serum (FBS), and analyzed by fluorescence-activated cell sorting (FACS) using a FACS Aria BDII. The analyses were carried out as described previously (*61*).

Pancreatic islet isolation

Pancreatic islets were isolated by collagenase digestion (0.9 U/ml) of mouse pancreata. Collagenase P (Sigma-Aldrich) was dissolved in cold RPMI and filtered through a 0.45-μm filter before use. Mice were euthanized by cervical dislocation, the common bile duct was clamped at the junction with the duodenum, and 3 ml of ice-cold collagenase/RPMI was injected in the common bile duct using a syringe with a 30-G needle until the pancreas was fully inflated. Pancreata were incubated for 18 min in warm RPMI at 37°C before being disrupted by hand shaking. Digested pancreata were passed through a 500-μm mesh before centrifugation at 193*g* for 5 min. Pooled acini and islet cells were washed twice with 50 ml of RMPI and centrifuged at 193*g* for 5 min. The pellet was resuspended in 10 ml of warm Histopaque-1077 (Sigma-Aldrich), overlayed with 5 ml of RPMI, and then centrifuged at 433*g* for 15 min with slow acceleration and without deceleration to generate a continuous density gradient. Islets were recovered at the interface between Histopaque-1077 and RPMI, transferred into 40 ml of RPMI, and centrifuged at 433*g* for 5 min. The cell pellets were suspended in 3 ml of CMRL media (Thermo Fisher Scientific) supplemented with 10% FBS, 1% penicillin and streptomycin (10,000 U/ml; Gibco), and 1% of 500× L-glutamine, and islets were plated in 60-mm petri dishes. The next day, the islets

were dispersed into single cells by trypsinization and plated in 24-well plates on glass slides for measurement of intracellular Ca^{2+} levels.

Calcium imaging and measurement

Intracellular calcium was monitored using the fluorescent indicator fura-2 as described previously (*62*). Ratiometric fluorescent (*R*) values were recorded on a Hamamatsu Orca ER digital camera attached to an inverted Nikon TE2000-U microscope at 1-min intervals with 50-ms exposure (excitation, 340/380 nm; emission, 510 nm). Metamorph 6.3 was used to quantify fluorescent signals by manually tracing pancreatic islet cells. An equivalent region not containing cells was used as background and was subtracted. At the end of each experiment, ionomycin (5 μM) and 5 mM Ca^{2+} were added to obtain R_{max}. Medium was then replaced with calcium-free imaging solution supplemented with EGTA (3 mM) to obtain R_{min}. Intracellular calcium $[Ca^{2+}]_i$ (nM) was calculated from ratiometric fluorescent values (*R*) according to the equation

$$[Ca]_i = K_d . b . (R - R_{min}) / (R_{max} - R)$$

where R_{min} = minimum ratiometric fluorescence value, R_{max} = maximum ratiometric fluorescent value, *b* (minimum fluorescence value at 380 nm/maximum fluorescent intensity at 380 nm), and K_d (dissociation constant) = 224 (nM) as determined previously (*63*).

Mitochondrial Ca^{2+} was monitored in pancreatic islet cells using the fluorescent indicator Rhod-2 (Thermo Fisher Scientific) as described previously (*64*, *65*). The cells were incubated in 140 mM NaCl, 5.4 mM KCl, 1.8 mM $CaCl_2$, 0.5 mM $MgCl_2$, and 5.5 mM Hepes (pH 7.4), supplemented with 1 μM Rhod-2 for 20 min at 37°C. The buffer was replaced with fresh prewarmed buffer and incubated for a further 30 min at 37°C. Fluorescent images were taken at 37°C before and after addition of 10 mM glucose using an Andor Zyla SCMOS 5.5 MP camera attached to an inverted Nikon TE2000-U microscope, driven by Metamorph 7.10 software (excitation, 545 nm; emission, 620 nm; interval, 0.5 min; exposure, 50 ms). At the end of each incubation, 5 μM ionomycin and 5 mM calcium were added to achieve maximum fluorescence (F_{max}). Once steady state was achieved, the buffer was removed and replaced with prewarmed calcium-free 140 mM NaCl, 5.4 mM KCl, 0.5 mM $MgCl_2$, 5.5 mM Hepes, 3 mM EGTA, and 11 mM glucose (pH 7.4) buffer, to achieve minimum fluorescence (F_{min}). Fluorescent images were quantified using Metamorph 7.10. The cells were manually traced to quantify the fluorescent signal. An equivalent area not containing cells was used as background and subtracted from matched cells. All responses were expressed as a percent increase from pretreatment (basal) fluorescent values (*F*) according to the following equation

$$\text{Rhod-2} = [(F - F_{min}) / (F_{max} - F_{min})]$$

Glucose stimulation of insulin secretion

The glucose stimulation of insulin secretion assay was performed 24 hours after the pancreatic islets from mouse were isolated and cultured in complete CMRL media [10% FBS, 1% penicillin and streptomycin (10,000 U/ml; Gibco), and 1% of 500× L-glutamine]. Ten islets per mouse were collected and transferred into a 24-well plate where they were washed twice with 0.5 ml of prewarmed Krebs buffer (pH 7.4) (137 mM NaCl, 4.7 mM KCl, 1.2 mM KH_2PO_4, 1.2 mM $MgSO_4$-$7H_2O$, 2.5 mM $CaCl_2$-$2H_2O$, 25 mM $NaHCO_3$, 10 mM Hepes, and 0.25% fat-free BSA). After the wash, the islets were incubated for 1 hour at 37°C with 200 μl of 5.5 mM glucose. The supernatant was collected, centrifuged at 376*g* for 5 min, and stored for determination of basal insulin content. The islets were then washed twice with 0.5 ml of Krebs buffer and incubated for 1 hour at 37°C with 200 μl of 16.7 mM glucose. The supernatant was collected, centrifuged at 376*g* for 5 min, and stored for determination of insulin secretion after glucose stimulation. The islets were then collected in 0.5 ml of Krebs buffer centrifuged at maximum speed for 5 min, and the pellet was stored for determination of insulin levels. Insulin levels were determined by using a commercial ELISA kit (Merck Millipore, EZRMI-13K), and the data were analyzed using an online software program (https://www.assayfit.com/).

Mitochondrial membrane potential measurements

Pancreatic islets were trypsinized to obtain single viable cells and seeded overnight in a black 96-well plate at a density of 12,500 cells per well in 200 μl of CMRL complete media. For each mouse, three wells were set up for FCCP treatment and six wells for nontreated cells. The next day, the islets were treated with 10 μl of 1 mM FCCP and placed for 10 min at 37°C, 5% CO_2. The medium was next removed and cells were washed twice with media not containing FBS. A fresh JC-1 50 μM staining solution was prepared on the day in Dulbecco's modified Eagle's medium in the absence of FBS and added at a volume of 50 μl per well to the same wells previously treated with FCCP and to untreated cells. Islets were then left in incubation for 1 hour protected from light at 37°C, 5% CO_2. After the staining solution was removed, the cells were washed with 200 μl of PBS/5% BSA and left at 5 min at 37°C. Next, the wash solution was removed and 100 μl of PBS was added per well before proceeding to the reading. Fluorescence emission was measured at 520/590 nm using a CLARIOstar plate reader.

Amino acid measurements

Amino acids were extracted in 50:50 water/methanol by homogenizing 20 mg of pancreas tissue or serum from *wt* and *N434S* mice fed on a NCD or a HFD, using a bead beater. The solvent was analyzed by targeted reversed-phase high-speed quantitative ultraperformance liquid chromatography–tandem mass spectrometry analysis as described previously (*66*).

SUPPLEMENTARY MATERIALS

Supplementary material for this article is available at https://science.org/doi/10.1126/sciadv.abi7514

View/request a protocol for this paper from *Bio-protocol*.

REFERENCES AND NOTES

1. A. Gonzalez-Franquesa, M.-E. Patti, Insulin resistance and mitochondrial dysfunction. *Adv. Exp. Med. Biol.* **982**, 465–520 (2017).
2. S. C. Johnson, B. Gonzalez, Q. Zhang, B. Milholland, Z. Zhang, Y. Suh, Network analysis of mitonuclear GWAS reveals functional networks and tissue expression profiles of disease-associated genes. *Hum. Genet.* **136**, 55–65 (2017).
3. N. Knoll, I. Jarick, A.-L. Volckmar, M. Klingenspor, T. Illig, H. Grallert, C. Gieger, H.-E. Wichmann, A. Peters, J. Hebebrand, A. Scherag, A. Hinney, Gene set of nuclear-encoded mitochondrial regulators is enriched for common inherited variation in obesity. *PLOS ONE* **8**, e55884 (2013).
4. J. M. Mercader, M. Puiggros, A. V. Segrè, E. Planet, E. Sorianello, D. Sebastian, S. Rodriguez-Cuenca, V. Ribas, S. Bonàs-Guarch, S. Draghici, C. Yang, S. Mora, A. Vidal-Puig, J. Dupuis; DIAGRAM Consortium, J. C. Florez; MITIN Consortium, A. Zorzano, D. Torrents, Identification of novel type 2 diabetes candidate genes involved in the crosstalk between the mitochondrial and the insulin signaling systems. *PLOS Genet.* **8**, e1003046 (2012).

5. D. C. Wallace, A mitochondrial paradigm of metabolic and degenerative diseases, aging, and cancer: A dawn for evolutionary medicine. *Annu. Rev. Genet.* **39**, 359–407 (2005).
6. A. Hodgkinson, Y. Idaghdour, E. Gbeha, J.-C. Grenier, E. Hip-Ki, V. Bruat, J.-P. Goulet, T. de Malliard, P. Awadalla, High-resolution genomic analysis of human mitochondrial RNA sequence variation. *Science* **344**, 413–415 (2014).
7. G. S. Gorman, P. F. Chinnery, S. Dimauro, M. Hirano, Y. Koga, R. McFarland, A. Suomalainen, D. R. Thorburn, M. Zeviani, D. M. Turnbull, Mitochondrial diseases. *Nat. Rev. Dis. Primers.* **2**, 16080–16022 (2016).
8. S. B. Vafai, V. K. Mootha, Mitochondrial disorders as windows into an ancient organelle. *Nature* **491**, 374–383 (2012).
9. D. Ojala, J. Montoya, G. Attardi, tRNA punctuation model of RNA processing in human mitochondria. *Nature* **290**, 470–474 (1981).
10. O. Rackham, T. R. Mercer, A. Filipovska, The human mitochondrial transcriptome and the RNA-binding proteins that regulate its expression. *WIREs RNA* **3**, 675–695 (2012).
11. J. Holzmann, P. Frank, E. Löffler, K. L. Bennett, C. Gerner, W. Rossmanith, RNase P without RNA: Identification and functional reconstitution of the human mitochondrial tRNA processing enzyme. *Cell* **135**, 462–474 (2008).
12. O. Rackham, J. D. Busch, S. Matic, S. J. Siira, I. Kuznetsova, I. Atanassov, J. A. Ermer, A.-M. J. Shearwood, T. R. Richman, J. B. Stewart, A. Mourier, D. Milenkovic, N.-G. Larsson, A. Filipovska, Hierarchical RNA processing is required for mitochondrial ribosome assembly. *Cell Rep.* **16**, 1874–1890 (2016).
13. S. J. Siira, G. Rossetti, T. R. Richman, K. Perks, J. A. Ermer, I. Kuznetsova, L. Hughes, A.-M. J. Shearwood, H. M. Viola, L. C. Hool, O. Rackham, A. Filipovska, Concerted regulation of mitochondrial and nuclear non-coding RNAs by a dual-targeted RNase Z. *EMBO Rep.* **19**, e46198 (2018).
14. M. D. Metodiev, K. Thompson, C. L. Alston, A. A. M. Morris, L. He, Z. Assouline, M. Rio, N. Bahi-Buisson, A. Pyle, H. Griffin, S. Siira, A. Filipovska, A. Munnich, P. F. Chinnery, R. McFarland, A. Rötig, R. W. Taylor, Recessive mutations in TRMT10C cause defects in mitochondrial RNA processing and multiple respiratory chain deficiencies. *Am. J. Hum. Genet.* **98**, 993–1000 (2016).
15. J. Zschocke, HSD10 disease: Clinical consequences of mutations in the HSD17B10 gene. *J. Inherit. Metab. Dis.* **35**, 81–89 (2012).
16. M. I. G. L. Sanchez, T. R. Mercer, S. M. K. Davies, A.-M. J. Shearwood, K. K. A. Nygård, T. R. Richman, J. S. Mattick, O. Rackham, A. Filipovska, RNA processing in human mitochondria. *Cell Cycle* **10**, 2904–2916 (2011).
17. E. Vilardo, C. Nachbagauer, A. Buzet, A. Taschner, J. Holzmann, W. Rossmanith, A subcomplex of human mitochondrial RNase P is a bifunctional methyltransferase—Extensive moonlighting in mitochondrial tRNA biogenesis. *Nucleic Acids Res.* **40**, 11583–11593 (2012).
18. S.-Y. Yang, X.-Y. He, H. Schulz, Multiple functions of type 10 17β-hydroxysteroid dehydrogenase. *Trends Endocrinol. Metab.* **16**, 167–175 (2005).
19. L. Reinhard, S. Sridhara, B. M. Hällberg, Structure of the nuclease subunit of human mitochondrial RNase P. *Nucleic Acids Res.* **43**, 5664–5672 (2015).
20. F. Li, X. Liu, W. Zhou, X. Yang, Y. Shen, Auto-inhibitory mechanism of the human mitochondrial RNase P protein complex. *Sci. Rep.* **5**, 9878 (2015).
21. T. Teramoto, K. J. Kaitany, Y. Kakuta, M. Kimura, C. A. Fierke, T. M. T. Hall, Pentatricopeptide repeats of protein-only RNase P use a distinct mode to recognize conserved bases and structural elements of pre-tRNA. *Nucleic Acids Res.* **48**, 11815–11826 (2020).
22. H.-H. Huang, L. Novikova, S. J. Williams, I. V. Smirnova, L. Stehno-Bittel, Low insulin content of large islet population is present in situ and in isolated islets. *Islets* **3**, 6–13 (2011).
23. D. B. Savage, K. F. Petersen, G. I. Shulman, Disordered lipid metabolism and the pathogenesis of insulin resistance. *Physiol. Rev.* **87**, 507–520 (2007).
24. H. V. Lin, A. Frassetto, E. J. Kowalik Jr., A. R. Nawrocki, M. M. Lu, J. R. Kosinski, J. A. Hubert, D. Szeto, X. Yao, G. Forrest, D. J. Marsh, Butyrate and propionate protect against diet-induced obesity and regulate gut hormones via free fatty acid receptor 3-independent mechanisms. *PLOS ONE* **7**, e35240 (2012).
25. H. Tilg, A. Kaser, Gut microbiome, obesity, and metabolic dysfunction. *J. Clin. Invest.* **121**, 2126–2132 (2011).
26. R. J. Perry, L. Peng, N. A. Barry, G. W. Cline, D. Zhang, R. L. Cardone, K. F. Petersen, R. G. Kibbey, A. L. Goodman, G. I. Shulman, Acetate mediates a microbiome–brain–β-cell axis to promote metabolic syndrome. *Nature* **534**, 213–217 (2016).
27. J. P. Silva, M. Köhler, C. Graff, A. Oldfors, M. A. Magnuson, P.-O. Berggren, N.-G. Larsson, Impaired insulin secretion and β-cell loss in tissue-specific knockout mice with mitochondrial diabetes. *Nat. Genet.* **26**, 336–340 (2000).
28. K. L. Perks, N. Ferreira, T. R. Richman, J. A. Ermer, I. Kuznetsova, A.-M. J. Shearwood, R. G. Lee, H. M. Viola, V. P. A. Johnstone, V. Matthews, L. C. Hool, O. Rackham, A. Filipovska, Adult-onset obesity is triggered by impaired mitochondrial gene expression. *Sci. Adv.* **3**, e1700677 (2017).
29. R. G. Lee, J. Gao, S. J. Siira, A.-M. Shearwood, J. A. Ermer, V. Hofferek, J. C. Mathews, M. Zheng, G. E. Reid, O. Rackham, A. Filipovska, Cardiolipin is required for membrane docking of mitochondrial ribosomes and protein synthesis. *J. Cell Sci.* **133**, jcs240374 (2020).
30. J. M. Baughman, F. Perocchi, H. S. Girgis, M. Plovanich, C. A. Belcher-Timme, Y. Sancak, X. R. Bao, L. Strittmatter, O. Goldberger, R. L. Bogorad, V. Koteliansky, V. K. Mootha, Integrative genomics identifies MCU as an essential component of the mitochondrial calcium uniporter. *Nature* **476**, 341–345 (2011).
31. A. Takeuchi, B. Kim, S. Matsuoka, The destiny of Ca^{2+} released by mitochondria. *J. Physiol. Sci.* **65**, 11–24 (2014).
32. S. Y. Yang, X. Y. He, D. Miller, Hydroxysteroid (17β) dehydrogenase X in human health and disease. *Mol. Cell. Endocrinol.* **343**, 1–6 (2011).
33. M. R. Alam, L. N. Groschner, W. Parichatikanond, L. Kuo, A. I. Bondarenko, R. Rost, M. Waldeck-Weiermair, R. Malli, W. F. Graier, Mitochondrial Ca^{2+} uptake 1 (MICU1) and mitochondrial Ca^{2+} uniporter (MCU) contribute to metabolism-secretion coupling in clonal pancreatic β-cells. *J. Biol. Chem.* **287**, 34445–34454 (2012).
34. D. Jiang, L. Zhao, C. B. Clish, D. E. Clapham, Letm1, the mitochondrial Ca^{2+}/H^{+} antiporter, is essential for normal glucose metabolism and alters brain function in Wolf–Hirschhorn syndrome. *Proc. Natl. Acad. Sci. U.S.A.* **110**, E2249–E2254 (2013).
35. A. G. McQuibban, N. Joza, A. Megighian, M. Scorzeto, D. Zanini, S. Reipert, C. Richter, R. J. Schweyen, K. A. Nowikovsky, A *Drosophila* mutant of LETM1, a candidate gene for seizures in Wolf–Hirschhorn syndrome. *Hum. Mol. Genet.* **19**, 987–1000 (2010).
36. M. Waldeck-Weiermair, C. Jean-Quartier, R. Rost, M. J. Khan, N. Vishnu, A. I. Bondarenko, H. Imamura, R. Malli, W. F. Graier, Leucine zipper EF hand-containing transmembrane protein 1 (Letm1) and uncoupling proteins 2 and 3 (UCP2/3) contribute to two distinct mitochondrial Ca^{2+} uptake pathways. *J. Biol. Chem.* **286**, 28444–28455 (2011).
37. Z. Fu, E. R. Gilbert, D. Liu, Regulation of insulin synthesis and secretion and pancreatic Beta-cell dysfunction in diabetes. *Curr. Diabetes Rev.* **9**, 25–53 (2013).
38. K. Nowikovsky, P. Bernardi, LETM1 in mitochondrial cation transport. *Front. Physiol.* **5**, 83 (2014).
39. C. Münch, J. W. Harper, Mitochondrial unfolded protein response controls matrix pre-RNA processing and translation. *Nature* **534**, 710–713 (2016).
40. C. Becker, A. Kukat, K. Szczepanowska, S. Hermans, K. Senft, C. P. Brandscheid, P. Maiti, A. Trifunovic, CLPP deficiency protects against metabolic syndrome but hinders adaptive thermogenesis. *EMBO Rep.* **19**, e45126 (2018).
41. H. Antonicka, Z.-Y. Lin, A. Janer, M. J. Aaltonen, W. Weraarpachai, A.-C. Gingras, E. A. Shoubridge, A high-density human mitochondrial proximity interaction network. *Cell Metab.* **32**, 479–497.e9 (2020).
42. A. E. Frazier, R. D. Taylor, D. U. Mick, B. Warscheid, N. Stoepel, H. E. Meyer, M. T. Ryan, B. Guiard, P. Rehling, Mdm38 interacts with ribosomes and is a component of the mitochondrial protein export machinery. *J. Cell Biol.* **172**, 553–564 (2006).
43. R. Durigon, A. L. Mitchell, A. W. Jones, A. Manole, M. Mennuni, E. M. Hirst, H. Houlden, G. Maragni, S. Lattante, P. N. Doronzio, I. Dalla Rosa, M. Zollino, I. J. Holt, A. Spinazzola, LETM1 couples mitochondrial DNA metabolism and nutrient preference. *EMBO Mol. Med.* **10**, e8550 (2018).
44. C. J. Lynch, S. H. Adams, Branched-chain amino acids in metabolic signalling and insulin resistance. *Nat. Rev. Endocrinol.* **10**, 723–736 (2014).
45. I. I. Nita, M. Hershfinkel, D. Fishman, E. Ozeri, G. A. Rutter, S. L. Sensi, D. Khananshvili, E. C. Lewis, I. Sekler, The mitochondrial Na^{+}/Ca^{2+} exchanger upregulates glucose dependent Ca^{2+} signalling linked to insulin secretion. *PLOS ONE* **7**, e46649 (2012).
46. N. Vishnu, A. Hamilton, A. Bagge, A. Wernersson, E. Cowan, H. Barnard, Y. Sancak, K. J. Kamer, P. Spégel, M. Fex, A. Tengholm, V. K. Mootha, D. G. Nicholls, H. Mulder, Mitochondrial clearance of calcium facilitated by MICU2 controls insulin secretion. *Mol. Metab.* **51**, 101239 (2021).
47. F. J. Clemente, A. Cardona, C. E. Inchley, B. M. Peter, G. Jacobs, L. Pagani, D. J. Lawson, T. Antão, M. Vicente, M. Mitt, M. DeGiorgio, Z. Faltyskova, Y. Xue, Q. Ayub, M. Szpak, R. Mägi, A. Eriksson, A. Manica, M. Raghavan, M. Rasmussen, S. Rasmussen, E. Willerslev, A. Vidal-Puig, C. Tyler-Smith, R. Villems, R. Nielsen, M. Metspalu, B. Malyarchuk, M. Derenko, T. A. Kivisild, Selective sweep on a deleterious mutation in CPT1A in arctic populations. *Am. J. Hum. Genet.* **95**, 584–589 (2014).
48. K. L. Perks, N. Ferreira, J. A. Ermer, D. L. Rudler, T. R. Richman, G. Rossetti, V. B. Matthews, N. C. Ward, O. Rackham, A. Filipovska, Reduced mitochondrial translation prevents diet-induced metabolic dysfunction but not inflammation. *Aging* **12**, 19677–19700 (2020).
49. A. Zisman, O. D. Peroni, E. D. Abel, M. D. Michael, F. Mauvais-Jarvis, B. B. Lowell, J. F. Wojtaszewski, M. F. Hirshman, A. Virkamaki, L. J. Goodyear, C. R. Kahn, B. B. Kahn, Targeted disruption of the glucose transporter 4 selectively in muscle causes insulin resistance and glucose intolerance. *Nat. Med.* **6**, 924–928 (2000).
50. T. R. Richman, O. Rackham, J. A. Ermer, S. M. K. Davies, K. L. Perks, H. M. Viola, A. Filipovska, A.-M. J. Shearwood, L. C. Hool, Mutation in MRPS34 compromises protein synthesis and causes mitochondrial dysfunction. *PLOS Genet.* **11**, e1005089 (2015).
51. I. V. Perevoshchikova, C. L. Quinlan, A. L. Orr, A. A. Gerencser, M. D. Brand, Sites of superoxide and hydrogen peroxide production during fatty acid oxidation in rat skeletal muscle mitochondria. *Free Rad. Biol. Med.* **61**, 298–309 (2013).

52. E. Ojuka, B. Andrew, N. Bezuidenhout, S. George, G. Maarman, H. P. Madlala, A. Mendham, P. O. Osiki, Measurement of β-oxidation capacity of biological samples by respirometry: A review of principles and substrates. *Am. J. Physiol.* **310**, E715–E723 (2016).
53. T. R. Richman, H. Spåhr, J. A. Ermer, S. M. K. Davies, H. M. Viola, K. A. Bates, J. Papadimitriou, L. C. Hool, J. Rodger, N.-G. Larsson, O. Rackham, A. Filipovska, Loss of the RNA-binding protein TACO1 causes late-onset mitochondrial dysfunction in mice. *Nat. Commun.* **7**, 11884 (2016).
54. F. Krueger, *Trim Galore: A wrapper tool around Cutadapt and FastQC* (2015); www.bioinformatics.babraham.ac.uk/projects/trim_galore/.
55. M. Martin, Cutadapt removes adapter sequences from high-throughput sequencing reads. *EMBnet J.* **17**, 10–12 (2011).
56. A. Dobin, C. A. Davis, F. Schlesinger, J. Drenkow, C. Zaleski, S. Jha, P. Batut, M. Chaisson, T. R. Gingeras, STAR: Ultrafast universal RNA-seq aligner. *Bioinformatics* **29**, 15–21 (2013).
57. H. Li, B. Handsaker, A. Wysoker, T. Fennell, J. Ruan, N. Homer, G. Marth, G. Abecasis, R. Durbin; 1000 Genome Project Data Processing Subgroup, The Sequence Alignment/Map format and SAMtools. *Bioinformatics* **25**, 2078–2079 (2009).
58. A. R. Quinlan, I. M. Hall, BEDTools: A flexible suite of utilities for comparing genomic features. *Nat. Commun.* **26**, 841–842 (2010).
59. J. M. Gaspar, NGmerge: Merging paired-end reads via novel empirically-derived models of sequencing errors. *BMC Bioinformatics* **19**, 536–539 (2018).
60. T. R. Richman, S. M. K. Davies, A.-M. J. Shearwood, J. A. Ermer, L. H. Scott, M. E. Hibbs, O. Rackham, A. Filipovska, A bifunctional protein regulates mitochondrial protein synthesis. *Nucleic Acids Res.* **42**, 5483–5494 (2014).
61. S. Matic, M. Jiang, T. J. Nicholls, J. P. Uhler, C. Dirksen-Schwanenland, P. L. Polosa, M.-L. Simard, X. Li, I. Atanassov, O. Rackham, A. Filipovska, J. B. Stewart, M. Falkenberg, N.-G. Larsson, D. Milenkovic, Mice lacking the mitochondrial exonuclease MGME1 accumulate mtDNA deletions without developing progeria. *Nat. Commun.* **9**, 1202 (2018).
62. H. M. Viola, S. M. K. Davies, A. Filipovska, L. C. Hool, L-type Ca^{2+} channel contributes to alterations in mitochondrial calcium handling in the mdx ventricular myocyte. *Am. J. Physiol. Heart Circ. Physiol.* **304**, H767–H775 (2013).
63. R. A. Haworth, D. Redon, Calibration of intracellular Ca transients of isolated adult heart cells labelled with fura-2 by acetoxymethyl ester loading. *Cell Calcium* **24**, 263–273 (1998).
64. A. Lombardi, J. Gambardella, X.-L. Du, D. Sorriento, M. Mauro, G. Iaccarino, B. Trimarco, G. Santulli, Sirolimus induces depletion of intracellular calcium stores and mitochondrial dysfunction in pancreatic beta cells. *Sci. Rep.* **7**, 15823–15829 (2017).
65. H. Lu, V. Koshkin, E. M. Allister, A. V. Gyulkhandanyan, M. B. Wheeler, Molecular and metabolic evidence for mitochondrial defects associated with beta-cell dysfunction in a mouse model of type 2 diabetes. *Diabetes* **59**, 448–459 (2010).
66. N. Gray, R. Zia, A. King, V. C. Patel, J. Wendon, M. J. W. McPhail, M. Coen, R. S. Plumb, I. D. Wilson, J. K. Nicholson, High-speed quantitative UPLC-MS analysis of multiple amines in human plasma and serum via precolumn derivatization with 6-Aminoquinolyl-N-hydroxysuccinimidyl Carbamate: application to acetaminophen-induced liver failure. *Anal. Chem.* **89**, 2478–2487 (2017).

Acknowledgments: We thank N. Larsson for valuable advice and critical reading of the manuscript, A.-M. Shearwood and N. Ferreira for technical assistance, and I. Atanassov and X. Li from the Proteomics Core Facility at the Max Planck Institute for Biology of Ageing for help with the proteomic analyses, the MGMP, and the APN node at Monash University for mouse embryo injections. **Funding:** This project was supported by fellowships and project grants from the NHMRC (to H.M.V., L.C.H., A.F., and O.R.), ARC (to A.F. and O.R.), CCWA (to O.R. and A.F.), Diabetes Research WA (to A.F., O.R., S.J.S., and J.A.E. and the Raine Medical Research Foundation (to T.R.R.). T.R.R. is a CSIRO/FSP Synthetic Biology Fellow and is supported by the Raine/Bright Spark Foundation. K.L.P. was supported by a Dora Lush NHMRC and AMDF scholarship. G.R. and L.A.H. are supported by UWA Postgraduate Scholarships. H.M.V. is a Heart Foundation Future Leader Fellow (101930). The APN is supported by the Australian Government Department of Education through the NCRIS, the Super Science Initiative, and the Collaborative Research Infrastructure Scheme. **Author contributions:** O.R. and A.F. conceived the project. O.R. and A.F. designed the experiments. All authors conducted and analyzed the experiments. G.R., O.R., and A.F. wrote the manuscript, and the other authors edited and approved the manuscript. **Competing interests:** The authors declare that they have no competing interests. **Data and materials availability:** All data needed to evaluate the conclusions in the paper are present in the paper and/or the Supplementary Materials. The Gene Expression Omnibus (GEO) accession number for the data reported in this paper is GSE162021.

Submitted 29 March 2021
Accepted 4 August 2021
Published 24 September 2021
10.1126/sciadv.abi7514

Citation: G. Rossetti, J. A. Ermer, M. Stentenbach, S. J. Siira, T. R. Richman, D. Milenkovic, K. L. Perks, L. A. Hughes, E. Jamieson, G. Xiafukaiti, N. C. Ward, S. Takahashi, N. Gray, H. M. Viola, L. C. Hool, O. Rackham, A. Filipovska, A common genetic variant of a mitochondrial RNA processing enzyme predisposes to insulin resistance. *Sci. Adv.* **7**, eabi7514 (2021).

ScienceAdvances

A common genetic variant of a mitochondrial RNA processing enzyme predisposes to insulin resistance

Giulia RossettiJudith A. ErmerMaike StentenbachStefan J. SiiraTara R. RichmanDusanka MilenkovicKara L. PerksLaetitia A. HughesEmma JamiesonGulibaikelamu XiafukaitiNatalie C. WardSatoru TakahashiNicola GrayHelena M. ViolaLivia C. HoolOliver RackhamAleksandra Filipovska

Sci. Adv., 7 (39), eabi7514. • DOI: 10.1126/sciadv.abi7514